MICHIGAN STATE UNIVERSITY

CYCLOTRON PROJECT

Studies of Beam Deflection for a Three-Sector Cyclotron*

J. W. Beal

ABSTRACT

STUDIES OF BEAM DEFLECTION
FOR A THREE-SECTOR CYCLOTRON

by Jack William Beal

Computer studies have been made of orbits in the deflector of a three-sector cyclotron; the results demonstrate the effects of the deflector mechanism under various conditions. Three basic deflector arrangements are considered with various channel field strengths: a continuous electrostatic channel; an electrostatic followed by a magnetic channel; and a single, 45° electrostatic channel. The studies demonstrate the effects of energy and azimuth at which deflection begins on deflector effectiveness and radial and axial focusing of the deflected beam. The results show that for a given channel apparatus and deflection energy, the deflector channel should start at the beginning of a magnet valley in order to minimize beam path length to the edge of the magnetic field. Furthermore, the optics of the deflected beam is sensitive to the azimuth and energy at which deflection begins and the beam path length during deflection. Additional studies show that the beam can be advantageously accelerated through the $\nu_r = 1$ resonance prior to deflection under proper conditions. In addition, the results demonstrate

ABSTRACT, continued

that the $\nu_r = 2\nu_z$ coupling resonance can be traversed without excessive instability.

STUDIES OF BEAM DEFLECTION

FOR A THREE-SECTOR CYCLOTRON

By

Jack William Beal

A THESIS

Submitted to
Michigan State University
in partial fulfillment of the requirements
for the degree of

DOCTOR OF PHILOSOPHY

Department of Physics and Astronomy

1964

ACKNOWLEDGMENTS

TABLE OF CONTENTS

LIST OF TABLES

LIST OF FIGURES

I. INTRODUCTION AND SUMMARY

This paper presents a survey of computer studies pertaining to the beam extraction system for a three-sector cyclotron. Prior to deflection turn separation must be generated in order that the beam clear the septum and enter the deflector channel. A study by Garren et.al. [Ref. 1] pertaining to the Berkeley 88-in. cyclotron surveyed conditions for which deflector channel acceptance efficiency is a maximum. Regarding the optimum parameters for the deflector, the study by Garren et.al. positioned the deflector at the azimuth where the equilibrium orbit radius gain per unit energy gain is greatest. A study for the Harwell cyclotron by Harragan et.al. [Ref. 2] used as a criterion ease of deflection in choosing the optimum deflector parameters. In the present paper it was desired to determine optimum deflector parameters in order to obtain rapid beam deflection and small beam spread at the edge of the main magnetic field. The first two sections of this work present a survey of deflection results and the third section presents overall extraction results for the M.S.U. cyclotron.

The primary requirements on the deflector are that it: (a) remove the internal beam from its nearly circular orbit and bend it out of the main magnetic field headed in the proper direction; (b) maintain good beam

optics; and (c) have sufficient aperture so as to transmit the desired current. In this study three basic deflector arrangements were studied: first, a long electrostatic channel that continued to the edge of the main magnetic field; second, a short electrostatic channel followed by a magnetic channel; and third, a single, 45° electrostatic channel. The objects of the deflection studies were to examine in detail the effect of the various choices of deflector channel apparatus and field strengths within the channel, the effect of initial deflector azimuth relative to the main magnetic field, and the effect of energy at which deflection occurs. By looking at orbit displacement and beam spread as a function of these parameters, conclusions can be made regarding the optimum azimuth at which to begin deflection, the conditions for minimum beam spread as the beam leaves the main magnetic field, and the minimum channel field strength required to produce the desired amount of deflection.

The computer studies reported herein were performed using the General Orbit Code with the Deflector Overwrite [Ref. 3]. In the computer code the effect of the deflector channel is represented by an appropriate modification of the main magnetic field. The effect of the electrostatic channel of constant electric field strength F is to subtract from the main magnetic field an equivalent

field F/v along the orbit where v is the particle velocity. In this manner it is assumed that the deflecting force is always perpendicular to the orbit.

First computations were made for static (non-accelerated) deflection. In the static deflection studies, orbits initially on the equilibrium orbit and on the linear eigen-ellipse about the E.O. representing the phase-space occupied by the beam were computed through the various deflector arrangements. The E.O. was chosen as the initial condition because it is a convenient reference orbit, and also, the accelerated orbits should remain close to the E.O. Also, the properties of the E.O. and the linear oscillations about the E.O. are well known [Refs. 4, 5]. Hereinafter, orbits initially on the equilibrium orbit at the entrance to the deflector will be called the central ray.

Initial studies were made using a three-sector magnetic field designed for 50 MeV protons. Values of energy chosen for study were 49 MeV (v_r = 0.901), 50 MeV (v_r = 0.821) and 51 MeV (v_r = 0.632) which cover the range of possible deflection energies. Values of electric field strength chosen for study were 100 and 150 kV/cm. For a 1 cm aperture these values cover the range from the relatively easy to obtain up to near the limiting

value due to sparking. A magnetic field strength of 4 kilogauss was studied for the magnetic channel. Four values of initial deflector azimuth were surveyed covering one sector (120°) in 30° steps.

For the continuous electrostatic channel the results indicate that minimum azimuthal length to the edge of the main magnetic field occurs by beginning deflection approximately 35° after a magnet hill or near the start of a magnet valley. This result is approximately 20° farther into the valley than the result obtained in the study by Harragan et.al. This difference is probably due to differences in the Harwell magnetic field and deflector arrangement. Since the effect of the channel field in changing the radius of curvature of the ion is greater in a valley than on a hill, it is expected that more rapid deflection would occur with deflection beginning near the start of a valley which the results indicate. In fact 120° after the start of deflection, central ray displacement is almost twice as great for deflection beginning 35° after a magnet hill instead of 25° before a hill. In addition the results demonstrate that an increase from 100 to 150 kV/cm electric field strength within the channel produces almost twice as much central ray displacement while a 1 MeV

increase in deflection energy yields approximately 15-20% more central ray displacement 120° after start of deflection.

Results on beam spread show that the final beam width varied by almost a factor of 2.5 over the range of initial deflector azimuths. Minimum beam width at the edge of the main magnetic field occurs by beginning deflection near the peak of a hill. This is the effect of postponing as long as possible the defocusing impulse due to the high radial gradient associated with the next succeeding hill field. Since the channel is flared so that the aperture increases as the beam spreads, the electric field cannot be uniform over the length of the channel. Studies show that under the best conditions the beam spreads from an initial width of about 0.2 in. to about 0.6-0.8 in. at the edge of the field, and it is doubtful that an electric field of 150 kV/cm can be maintained across the outer end of such a channel. Studies of axial motion within the deflector channel indicate that axial focusing is not a problem since the field is falling in the edge region.

The second set of deflection studies was for an electrostatic channel followed by a magnetic channel. The problem of achieving sufficient channel aperture

so as to accommodate the beam spread can be solved by using a magnetic channel near the end of the deflection process. Furthermore, the 4 kilogauss channel yields a deflecting force approximately 2.5 times stronger than a 150 kV/cm electrostatic channel, thus the beam is deflected more rapidly. Results are presented pertaining to achieving sufficient clearance for insertion of the magnetic channel.

For the single, 45° electrostatic channel approximately 30° more arc around the cyclotron is required before the beam is out to the edge of the main magnetic field. Since the beam travels for a longer period in the edge region of the field, beam spread for the 45° electrostatic channel is considerably greater than either the continuous electrostatic channel or the combined electrostatic and magnetic channel deflection system. Such deflectior would be feasible only if a focusing element can be inserted along the deflection path.

A set of computer runs was made to study the effect upon deflection of particle rotation with respect to the magnet spiral. These results indicate that for weak spiral fields the direction of rotation is not a significant factor for purposes of deflection.

A series of computer runs was made to study the variable-energy, multi-particle aspect of the cyclotron with respect to deflection. In these studies low energy protons and high energy C^{4+} ions were tracked through the deflector in order to compare central ray displacement with the high energy proton deflection. By choosing the energy at which deflection occurs so as to have the initial radii of the orbits coincide and then varying the field strength within the channels, the orbits could be matched quite closely over the length of the channel. This indicates that for the M.S.U. cyclotron the magnetic field shape is nearly independent of excitation in the extraction region. These deflection results indicate that operation in variable-energy, multi-particle modes can be accomplished by a simple change in channel field strengths without any change in deflector shape or position.

In the final section of this paper results are presented pertaining to the overall beam extraction process for the M.S.U. cyclotron. This section is a continuation and extension of a previous study by Gordon and Blosser [Ref. 6].

Median plane results are presented showing that the beam can be advantageously accelerated through the $\nu_r = 1$

resonance under the proper conditions. With no field bump in place, there is no turn separation generated on successive turns near the deflection point. Using the method of resonant extraction with a 1.0 gauss field bump in place, a 0.05 in. turn separation is generated thereby making insertion of the septum feasible. In addition the results show that phase-space distortion remains quite small for acceleration through the resonance under these conditions.

Results are presented showing that it is advantageous to accelerate into the non-isochronous region even though the phase is slipping quite rapidly. The results show that the E.O. radius gain and also the radius gain due to the precessional motion are both considerably larger in the edge region even though the energy gain per turn drops to approximately half its maximum value.

The orbits obtained by acceleration out to the deflection point were then studied through various deflector arrangements. These studies were made in order to gain more specific information for design of the M.S.U. cyclotron deflection system. The choice for deflector parameters for the M.S.U. cyclotron is a 60°, 120 kV/cm electrostatic channel followed by a 7.5° coasting period

and a 37.5°, 3 kilogauss magnetic channel.

Studies of combined axial and radial motion were made to observe the effects of the coupling resonances. Since the $\nu_r = 2\nu_z$ resonance is the lowest order coupling resonance traversed, it is expected that the instabilities associated with this resonance will be more serious than those due to the higher order resonances.

Using a special computer program, results of the coupled motion were obtained indicating that the $\nu_r = 2\nu_z$ resonance can be traversed under the proper conditions. However, the amount of axial instability is quite sensitive to the orbit center displacement. Due to the coupling effect with a maximum z-amplitude of 0.5 in. the radial beam width at the entrance to the deflector is "smeared" to approximately 40% greater width than that obtained for median plane motion. These results indicate that it is necessary to restrict the axial width in order to obtain real turn separation at the entrance to the deflector.

II. STATIC DEFLECTION

These studies were made for static (non-accelerated)
orbits in order to gain information on the deflection pro-
cess as a function of channel field strength and deflector
channel apparatus, initial deflector azimuth relative to
the main magnetic field, and energy at which deflection
occurs. For these studies, orbits initially on the equi-
librium orbit and on the linear eigen-ellipse representing
the phase-space occupied by the beam about the E.O. were
tracked through the various deflector channels under var-
ious conditions. In this manner the effect of the vari-
ables on resultant beam displacement and beam spread could
be studied.

The basic deflector mechanism can be understood quali-
tatively by the following simple analysis. Since the hill
field is much stronger and has a larger radial field gra-
dient than the valley field, the deflector would be more
efficient if it could bend the beam away from the hill
field into the rapidly decreasing edge region. This would
indicate beginning the deflector near the start of a magnet
valley and deflecting as sharply as possible before the
beam reaches the next hill. Since the momentum, p, is
constant, then:

$$p = qB(r,\theta)\rho_O(r,\theta) \; ; \tag{1}$$

where $B(r,\theta)$ is the magnetic field along the equilibrium orbit and $\rho_O(r,\theta)$ is the radius of curvature of the E.O. Rewriting Eq. (1) to include motion within the deflector channel yields:

$$p = q \left[B(r,\theta) - \delta r \left| \frac{\partial B}{\partial r} \right| - \frac{F}{v} \right] [\rho_O(r,\theta) + \delta\rho] \; , \tag{2}$$

where $\delta\rho$ is the change in the radius of curvature due to the deflector mechanism, δr is the displacement from the E.O., v is the velocity of the particle; and it is assumed that the deflecting electric field, F, acts perpendicular to the orbit. Expanding Eq. (2) and keeping only first order terms yields:

$$\frac{\delta\rho}{\rho_O} = \frac{\delta r}{B(r,\theta)} \left| \frac{\partial B}{\partial r} \right| + \frac{F}{B(r,\theta)v} \; . \tag{3}$$

From the second term on the right of Eq. (3), it is seen that for a given electric field strength within the channel and a given energy the fractional change in the radius of curvature of the orbit is greater in a magnet valley than on a magnet hill since $1/B$ is greater in a valley. The effect of the first term on the right of

Eq. (3) is most important when the orbits cross the hill since $\left|\frac{\partial B}{\partial r}\right|$ is much greater on a hill than anywhere else. It appears advantageous, from the standpoint of speed of deflection, to begin deflection near the start of a magnet valley since beam displacement, δr, will then be greatest as the particle crosses the hill. In this manner the effects of both terms of Eq. (3) are employed advantageously.

To study the effects of beam spread, consider the linear differential equation for a particle displaced from a given orbit:

$$\rho^2 \frac{d^2\xi}{ds^2} + (1-n)\xi = 0 \; ; \tag{4}$$

where ρ is the radius of curvature of the central ray, ξ is the displacement normal to the central ray, s is the arc length along the central ray, and $n = -\frac{\rho}{B}\frac{\partial B}{\partial \xi}$ evaluated along the central ray. Since the field gradient is large across the edge of a magnet hill compared to a valley, displaced orbits experience a radially defocusing impulse in this region. This would indicate beginning the deflector near the peak of a hill so as to have the next succeeding defocusing region as far away as possible thus placing the defocusing impulse near the end of deflection.

For computational purposes the high energy proton magnetic field designated 187F6 was used in these studies. This is a three-sector magnetic field with initial data taken from a set of magnet measurements designated Run 187. The properties of this field have been reported in detail by Blosser [Ref. 7]. The 187F6 field closely resembles the magnetic field adopted for the M.S.U. cyclotron. Figure 1 is a contour map of the magnetic field drawn directly from measured data. Also, the datum $\theta = 0°$ is shown and the 49 MeV ($\nu_r = 0.901$) proton equilibrium orbit is shown by the heavy dashed line. This field is a high excitation field yielding proton equilibrium orbits up to approximately 51.40 MeV. Table 1 presents equilibrium orbit data for the 187F6 field. The measured data on the 187F6 field allow orbits to be computed out to a radius of 45 in.; for comparison the last circulating orbit has a radius of approximately 29 in. while the nominal cyclotron radius is 32 in. At 45 in. the average magnetic field is down to about 2 kilogauss. Hereinafter, this 45 in. radius will be referred to as the "edge of the magnetic field."

A. Continuous Electrostatic Deflection

The first series of computer studies was made for a long electrostatic channel that continued to the edge of the magnetic field. In this manner, central ray deflection could be investigated as a function of electric field strength, F, within the channel, initial deflector azimuth, θ_o, and energy, E, at which deflection occurs. The 49 MeV equilibrium orbit has a maximum value of $r(\theta)$ at approximately 70°; this azimuth is considered to be the location of a hill. The initial deflector azimuths are: $\theta_o = 15°$, beginning deflection near the center of the valley; $\theta_o = 45°$, beginning deflection about halfway up the hill; $\theta_o = 75°$, beginning deflection near the peak of the hill; and $\theta_o = 105°$, beginning deflection about halfway down the hill. Electric field strengths of 100 and 150 kV/cm were chosen for study. For a 1 cm aperture these values cover the range from the relatively easy to obtain up to near the maximum due to sparking ($VF \doteq 10^{10}$ volts^2/cm). Deflection energies of 49, 50 and 51 MeV were chosen for study; these energies cover the range of ν_r values from 0.901 to 0.632.

The results given in Tables 2a, b, c and Fig. 2 present Δr vs. $\Delta \theta$ for values of F, θ_o and E where:

$$\Delta r = r_c - r_e \; ;$$

(5)

$$\Delta \theta = \theta - \theta_o \; .$$

$r_c(\theta)$ is the coordinate of the central ray, and $r_e(\theta)$ is the coordinate of the E.O. at the particular θ. The results indicate that for a given electric field and energy, in order to reach the edge of the magnetic field in the shortest $\Delta \theta$, a value of $\theta_o \doteq 105°$, or $35°$ beyond the hill, would be the optimum initial azimuth of the deflector. Typical results of central ray displacement for the case of $F = 150$ kV/cm and $E = 50$ MeV $60°$ after start of deflection are 1.70 in. for $\theta_o = 105°$ compared to 1.91 in. for $\theta_o = 45°$. $120°$ after start of deflection for the same energy and electric field, the central ray displacement is 12.96 in. for $\theta_o = 105°$ compared with 6.84 in. for $\theta_o = 45°$; i.e., the deflector azimuth which maximizes Δr depends on the $\Delta \theta$ at which Δr is evaluated. This result is an indication of the relative importance of the two terms on the right of Eq. (3).

For a given θ_o and energy, an increase from 100 to 150 kV/cm requires approximately $22°$ less arc around the machine to reach the edge of the magnetic field. At $\Delta \theta = 120°$ and for a given θ_o and energy, an increase to

the higher electric field yields approximately twice as much central ray displacement. For a fixed θ_o and electric field strength, a 1 MeV (or about 2%) increase in deflection energy yields 15-20% more central ray displacement at $\Delta\theta = 120°$.

The next study for the continuous electrostatic channel arrangement was the consideration of beam spread. The amount of beam spread determines the necessary width of the channel and also the aperture of any focusing elements used after deflection. Let x be the radial displacement and p_x its conjugate momentum relative to the equilibrium orbit. Beam spread considerations were then investigated by tracking through the deflector a group of orbits whose coordinates, (x, p_x), occupy eigen-ellipses about the E.O. of constant area normalized to a radial beam width $\Delta x = 0.2$ in. at $\theta = 0°$ and 50 MeV. The eigen-ellipse is defined by eight (x, p_x) points about the central ray. The eigen-ellipses for 49 and 51 MeV at $\theta = 0°$ were normalized to have phase-space areas equal to that for 50 MeV. Initial beam width for the 49-MeV case is approximately 10% less than that for 50 MeV; while for the 51-MeV case, initial beam width is approximately 19% greater than that for 50 MeV. This result follows from the qualitative relation between the width

of the eigen-ellipse and the E.O. properties; namely:

$$\Delta x^2 \propto \frac{R}{p\nu_r} ; \tag{6}$$

where Δx is the radial width of the eigen-ellipse, R is the mean radius of the equilibrium orbit, p is the momentum and ν_r is the frequency of the radial oscillations. Since ν_r and p/R are decreasing in the edge region where deflection is to take place, the beams exhibits adiabatic "undamping" or expansion at the higher energies. Therefore, deflection at the higher energies would require a larger channel aperture.

Define ξ as the displacement normal to the velocity of the central ray; the value of ξ is calculated by the approximate relation:

$$\xi = \frac{(r-r_c)\cos\alpha}{\cos(\alpha-\beta)} ; \tag{7}$$

with:
$$\sin\alpha = \frac{p_r}{p} ; \quad \sin\beta = \frac{p_{r_c}}{p} ;$$

where (r, p_r) are the coordinates of the particular orbit, (r_c, p_{r_c}) are the coordinates of the central ray at that θ, and p is the (constant) momentum. Eq. (7) is approximate in that no change in curvature over a small distance of

order $(r-r_c)\sin\beta$ is assumed. If r_1 and r_2 denote respectively the outermost and innermost radii of the group of eight orbits tracked, then the perpendicular beam width, $\Delta\xi$ is given by:

$$\Delta\xi = \xi_1 - \xi_2 .\qquad\qquad(8)$$

Tables 3a, b, c and Fig. 3 present results of $\Delta\xi$ vs. $\Delta\theta$ for values of θ_o, F and E. As expected, the results for $\Delta\xi$ indicate that minimum final beam width is obtained with deflection beginning near the peak of a hill. Typical values of beam width at the edge of the magnetic field for the case of $F = 150$ kV/cm and $E = 50$ MeV are 1.47 in. ($\Delta r = 12.89$ in.) for deflection beginning at $\theta_o = 15°$ compared to 0.57 in. ($\Delta r = 12.21$ in.) for deflection beginning at $\theta_o = 75^c$ which is a factor of approximately 2.5 difference in width. From the results it is seen that $\Delta\xi$ increases rather slowly until the beam crosses a hill and then increases rather rapidly thereafter. At the edge of the magnetic field and for a given E and θ_o, $\Delta\xi$ is approximately 20% less for deflection by the higher electric field strength. This result is due to the fact that the beam travels a shorter time in the edge field with the higher electric field in place. It should be noted

that the results assume an initial radial spread of 0.2 in.
However, the relative changes in $\Delta \xi$ obtained should be
reasonably accurate.

Consider next the question of beam optics. Figure 4
shows typical $r - p_r$ phase plots, at several $\Delta \theta$ values,
for the radial eigen-ellipse tracked through the contin-
uous 150 kV/cm electrostatic channel with $\theta_o = 75°$ and
E = 50 MeV. As can be seen from the figure, the radial
phase-space remains a reasonably compact and undistorted
figure and is well-centered about the central ray. From
this it can be concluded that the non-linear effects are
quite small.

Axial focusing in the deflection process was checked
in a series of computer runs similar to those for the
radial motion. Since the magnetic field is decreasing
rapidly in the edge region, axial focusing is increasing,
and it is expected that no problem with the axial motion
will be encountered. The axial equations of motion are,
of course, symmetric about the median plane, so that only
half the axial eigen-ellipse need be computed with the
mirror image of each point giving the remainder of the
phase-space figure. The (z, p_z) eigen-ellipses were nor-
malized to $\Delta z = 0.2$ in. at $\theta = 0°$ and at 50 MeV with
eigen-ellipses at 49 and 51 MeV having phase-space areas

equal to that at 50 MeV, each axial eigen-ellipse having radial coordinates corresponding to the central ray at the particular energy. Figure 5 shows results of $|z_{max}|$ vs. $\Delta\theta$ for values of θ_o, F and E as noted. $|z_{max}|$ is the maximum axial displacement of the four (z,p_z) orbits. From Fig. 5, it is seen that for a fixed θ_o the curves differ slightly as a function of electric field and energy. The decrease in initial axial width at higher energies is due to the adiabatic damping of the axial motion. The main variation in the curves arises through variations in θ_o. This is due to the sector structure in the magnetic field. It is seen that the axial motion undergoes a focusing impulse as it passes a hill region. For example, for deflection beginning at $\theta_o = 105°$, the next succeeding magnet hill peak is at $\Delta\theta = 85°$. From the figure, it is seen that the axial width undergoes a focusing impulse at approximately this point with the minimum axial width occurring about 20° after the peak of the hill.

Phase plots, at several $\Delta\theta$ values, for the axial eigen-ellipse tracked through the continuous 150 kV/cm electrostatic channel with $\theta_o = 75°$ and E = 50 MeV (same parameters as $r - p_r$ phase plots of Fig. 4) are shown in Fig. 6. The points on the axial eigen-ellipse

are associated with the 50 MeV central ray. From the figure, it is seen that the ellipse is merely rotating and changing shape. This is the result since the computer code integrates linear axial equations of motion.

Another factor determined for the continuous electrostatic channel was the arc length, Δs, along the central ray necessary to produce a given central ray displacement. In this manner an indication of the actual channel length required could be obtained. Table 4 tabulates results for Δs as a function of θ_o, F and E, necessary to produce a displacement of $\Delta r = 10.90$ in. The results indicate that in order to minimize the length of the channel for a given electric field strength and deflection energy, the deflector should start near the beginning of a magnet valley. Deflection at the higher energies and higher electric field strength reduces the length of the electrostatic channel required. The results for Δs are comparable to those obtained previously for the shortest $\Delta\theta$ to reach the edge of the field.

The continuous electrostatic channel to the edge of the field is a simple configuration to compute and analyze but does not necessarily represent a feasible situation. It does, however, furnish a basis for evaluation

of different parameters and also a basis for comparing
other channel arrangements.

B. <u>Electrostatic and Magnetic Channel Deflection</u>

Computer studies of an electrostatic deflector fol-
lowed by a magnetic channel were made using the same
initial conditions as those in the previous section. For
these studies a 60° electrostatic channel with a field
strength of 150 kV/cm was assumed, followed by a 7.5°
coasting period, followed by a 4 kilogauss magnetic
channel which continued to the edge of the magnetic
field. Energies of 50 and 51 MeV were chosen for this
study. For values of $\Delta\theta \leq 60°$, resultant Δr and $\Delta\xi$
values are the same as those of the previous section for
the same values of energy and initial deflector azimuth.

Table 5 presents results on Δr vs. $\Delta\theta$ for the
electrostatic and magnetic channel deflection arrangement.
The results, as a function of θ_o and E, are seen to be
similar to those for the continuous electrostatic channel
of the preceding section. Since the 4 kilogauss magnetic
channel is about 2.5 times stronger than a 150 kV/cm
electrostatic channel for 50 MeV protons, deflection with
this magnetic channel is more rapid requiring approximately

10° less arc to reach the edge of the magnetic field.
Table 6 presents results for $\Delta\xi$ vs. $\Delta\theta$ for the electrostatic and magnetic channel deflection system. The results are much the same as in the preceding section except that the beam spread is smaller reflecting the fact that the beam travels in the edge field for a shorter time. Tabulated below is a comparison, at the end of the magnetic field, between the continuous 150 kV/cm electrostatic channel and the 150 kV/cm electrostatic channel followed by a 4 kilogauss magnetic channel for the 50-MeV case with $\theta_o = 105°$.

	cont. elec.	elec. and mag.
Δr	12.96 in.	12.52 in.
$\Delta\xi$	0.85 in.	0.69 in.
$\Delta\theta$	120°	112.5°

A set of computer studies was made to survey various combinations of electrostatic and magnetic channels specifically for the case of the M.S.U. cyclotron. These studies were made in order to investigate the possibility of using a shorter electrostatic channel and a different initial azimuth θ_{om} for the magnetic channel. The primary requirement is that the beam come out of

the vacuum tank in the desired location. Furthermore, at least a 1.5 in. central ray displacement was deemed necessary for insertion of the magnetic channel. For these studies, a value of θ_o = 97.5° was used; this choice is based on the results described above in combination with constraints of the mechanical design for the M.S.U. cyclotron.

Two deflection systems were considered: first, a 60°, 150 kV/cm electrostatic channel followed by a 7.5° coasting period and then a 4 kilogauss magnetic channel to the edge of the magnetic field; and second, a short 37.5°, 150 kV/cm electrostatic channel with the beam then coasting around to various θ_{om} values where a 4 kilogauss magnetic channel was then assumed in place. The 37.5° channel length was investigated because such a channel could be positioned in the 42° wide dummy dee region between the two dees for the M.S.U. cyclotron. Such a positioning would eliminate the problem of providing insulation space for the electrostatic channel.

Figures 7 and 8 depict respectively the 51 and 50 MeV central rays through the various deflectors plotted on the schematic of the M.S.U. cyclotron. The central rays are initially on their respective equilibrium orbits at θ_o = 97.5°. In the figures curve "a" depicts

the 37.5°, 150 kV/cm electrostatic channel followed by a
45° coasting period with θ_{om} = 180°; curve "b" depicts
the 37.5° channel followed by a 37.5° coasting period
with θ_{om} = 172.5°; curve "c" depicts the 37.5° channel
followed by a 30° coasting period with θ_{om} = 165°;
curve "d" depicts the 37.5° channel followed by a 22.5°
coasting period with θ_{om} = 157.5°; curve "e" depicts
the 60° electrostatic channel followed by a 7.5° coast-
ing period with θ_{om} = 165°. Case "e" is one of the
channel configurations investigated above and served
as a basis for comparison.

For 51 MeV with the 37.5° electrostatic channel,
and initial azimuths of the magnetic channel $\theta_{om} \gtrsim 180°$
(curve "a"), the deflection was not sufficient to bend
the beam clear of the vacuum chamber in the region de-
sired. For the 50-MeV case with the 37.5° electrostatic
channel and initial magnetic channel azimuths
$\theta_{om} \gtrsim 170°$ (curve "b"), the deflection was again not suf-
ficient to bend the beam clear of the vacuum chamber.
For case "e" (the 60° electrostatic channel with the
magnetic channel beginning at θ_{om} = 165°), deflection
was more rapid than for any of cases a-d.

Regarding the second requirement of generating suf-
ficient beam displacement in order to insert the magnetic

channel, case e for the 60° electrostatic channel produces a central ray displacement, at $\theta_{om} = 165°$, of approximately two inches for both energies. In cases a-d for the 37.5° electrostatic channel, the beam must coast for a distance before the required displacement is attained. In the 51-MeV case depicted in Fig. 7, only values of $\theta_{om} \gtrsim 155°$ (curve "d") satisfied the 1.5 in. central ray displacement requirement. Therefore, for 51 MeV central ray deflection with a 37.5°, 150 kV/cm electrostatic channel, $155° \leq \theta_{om} \leq 180°$ limits the initial azimuth of the magnetic channel under these conditions. Similar results for the 50-MeV case with the 37.5° electrostatic channel showed that the initial azimuth of the magnetic channel is limited to values $160° \leq \theta_{om} \leq 170°$.

The above results indicate that deflection can be accomplished by using a suitable combination of electrostatic and magnetic channels. The two requirements of beam displacement for insertion of the magnetic channel and deflection of the beam into the region desired specify limits as to the position of the magnetic channel.

C. Short Electrostatic Channel

Studies of deflection by means of a short electrostatic channel were made using the same initial conditions as in Sec. A above. For this deflection system a single, 45° electrostatic channel was assumed with the beam then coasting to the edge of the magnetic field. The 45° channel length was investigated because such a channel could be positioned in the dummy dee region between the two dee stems thus eliminating problems of providing insulation space. With the short electrostatic channel, deflection is, of course, not nearly as rapid; and since the beam travels a relatively long period in the edge field, the beam width is greater than that for the more rapid deflection methods described above.

Computations were limited to values of $E = 50$ MeV and $F = 150$ kV/cm. Table 7 presents results of Δr vs. $\Delta\theta$ and $\Delta\xi$ vs. $\Delta\theta$ for various θ_0 values. These results should be compared with Tables 2b and 3b above. For the 45° electrostatic channel, approximately 30° more arc around the cyclotron would be required before the beam is as far out in the edge field as it would be in the continuous electrostatic channel case. At the edge of the magnetic field and for a fixed θ_0, $\Delta\xi$ for the 45° electrostatic channel is increased by approximately a factor of two over that for the continuous electrostatic channel.

The single, 45° electrostatic deflector is clearly the simplest of the three deflection systems considered. However, such a deflection system is not feasible unless a focusing element can be inserted along the deflection path in order to reduce the radial beam spread. Such a focusing element has been used in the Philips 30 MeV cyclotron [Ref. 8].

D. Deflection with Particle Rotation Against the Spiral

A set of computer runs was made to determine whether or not the direction of particle rotation with respect to the spiral has a significant effect on the deflection process. Referring to Fig. 1, it is seen that the magnetic field employed has comparatively little spiral. Using an energy of 50 MeV and with a continuous 150 kV/cm electrostatic channel, studies were made for deflection with rotation against the spiral to compare with those for rotation with the spiral (Sec. A).

In order to make the initial θ_o' values for the backwards runs (against the spiral) match those for forward runs (with the spiral) with respect to the hill and valley positions, set $\theta_o' = 2\theta_{hill} - \theta_o$. Using $\theta_{hill} = 67.5°$, values of θ_o' determined in this manner are $\theta_o' = 0°$, $90°$,

$60°$, $30°$ which correspond respectively to $\theta_o = 15°$, $45°$, $75°$, $105°$ of the previous studies. Table 8 presents results of Δr vs. $\Delta \theta$ and $\Delta \xi$ vs. $\Delta \theta$ for values of θ_o' for the case of rotation against the spiral. It can be seen by comparing Table 8 with Tables 2b and 3b that Δr is approximately 10% less and $\Delta \xi$ is approximately 10% greater than that obtained for rotation with the spiral. However, the general features of Δr and $\Delta \xi$ as a function of θ_o are comparable for the two directions of rotation.

Table 1. Equilibrium orbit data for 187F6 magnetic field.

E(MeV)	$R_{ave.}$(in)	ν_r	ν_z
40	25.59	1.0443	.1678
41	25.90	1.0426	.1704
42	26.20	1.0399	.1808
43	26.51	1.0350	.2038
44	26.81	1.0270	.2408
45	27.11	1.0179	.2807
46	27.42	1.0032	.3375
47	27.73	.9812	.4095
47.5	27.89	.9664	.4522
48	28.06	.9486	.4987
48.5	28.23	.9282	.5478
49	28.41	.9009	.6047
49.5	28.61	.8669	.6679
50	28.82	.8206	.7416
50.5	29.06	.7526	.8355
51	29.37	.6316	.9656
51.2	29.54	.5396	1.0426
51.4	29.91	.1794	1.2258

Table 2a. Δr vs. Δθ (see Eq. (5)) for continuous channel. E = 49 MeV, Δr = in.

θ° / Δθ	100 (kV/cm)				150 (kV/cm)			
	15°	45°	75°	105°	15°	45°	75°	105°
30°	.283	.306	.296	.264	.427	.460	.444	.397
45°	.646	.688	.610	.605	.980	1.041	.919	.915
60°	1.173	1.194	1.002	1.097	1.802	1.825	1.514	1.675
75°	1.890	1.687	1.547	1.750	2.980	2.619	2.358	2.732
90°	2.779	2.149	2.258	2.664	4.593	3.388	3.519	4.351
105°	3.585	2.762	3.237	4.004	6.471	4.431	5.341	7.007
120°	4.243	3.603	4.793	5.929	8.658	6.072	8.593	11.397
127.5°	4.626	4.192	5.925	7.083	10.051	7.388	11.134	14.526
135°	5.091	4.985	7.399	8.352	11.844	9.251	14.625	
142.5°	5.683	6.055	9.295	9.773	14.347	11.867		
150°	6.506	7.493	11.699	11.425		15.569		
157.5°	7.702	9.430	14.730	13.453				
165°	9.415	12.036		16.128				
172.5°	11.818	15.533						
180°	15.181							

Table 2b. Δr vs. Δθ (see Eq. (5)) for continuous electrostatic channel. E = 50 MeV, Δr = 1in.

θ° / Δθ	100 (kV/cm)				150 (kV/cm)			
	15°	45°	75°	105°	15°	45°	75°	105°
30°	.286	.310	.300	.267	.431	.466	.450	.401
45°	.658	.705	.620	.610	.999	1.068	.935	.923
60°	1.214	1.242	1.015	1.111	1.869	1.907	1.538	1.698
75°	2.004	1.782	1.563	1.803	3.173	2.797	2.389	2.825
90°	3.046	2.285	2.298	2.825	5.069	3.680	3.600	4.632
105°	4.117	2.946	3.378	4.407	7.526	4.870	5.609	7.703
120°	5.128	3.902	5.179	6.817	10.734	6.843	9.290	12.961
127.5°	5.716	4.615	6.521	8.373	12.887	8.478	12.206	
135°	6.431	5.601	8.291	10.196	15.764	10.814		
142.5°	7.375	6.947	10.603	12.359		14.138		
150°	8.722	8.775	13.603	15.016				
157.5°	10.688	11.264						
165°	13.519	14.665						

Table 2c. Δr vs. $\Delta \theta$ (see Eq. (5)) for continuous electrostatic channel. $E = 51$ MeV, $\Delta r = 1$ in.

$\Delta\theta$ \ θ_0	100 (kV/cm)				150 (kV/cm)			
	15°	45°	75°	105°	15°	45°	75°	105°
30°	.292	.318	.308	.273	.441	.479	.463	.410
45°	.682	.737	.644	.623	1.036	1.117	.973	.943
60°	1.290	1.334	1.055	1.143	1.990	2.051	1.603	1.749
75°	2.205	1.978	1.623	1.907	3.501	3.137	2.492	2.997
90°	3.517	2.601	2.418	3.110	5.852	4.301	3.818	5.105
105°	5.115	3.407	3.690	5.080	9.269	5.870	6.174	8.821
120°	6.955	4.662	5.922	8.274	14.312	8.618	10.610	15.461
127.5°	8.074	5.671	7.623	10.485		10.959	14.192	
135°	9.466	7.085	9.898	13.232		14.357		
142.5°	11.357	9.038	12.931	16.707				
150°	14.089	11.726						

Table 3a. Δξ vs. Δθ (see Eqs. (7), (8)) for continuous electrostatic channel. E = 49 MeV, Δξ = 1in.

Δθ \ θ	100 (kV/cm)				150 (kV/cm)			
	15°	45°	75°	105°	15°	45°	75°	105°
30°	.157	.168	.195	.170	.158	.170	.197	.172
45°	.157	.186	.197	.148	.162	.192	.201	.151
60°	.186	.215	.178	.160	.200	.231	.184	.166
75°	.230	.231	.155	.184	.269	.265	.163	.204
90°	.295	.222	.167	.232	.395	.280	.180	.289
105°	.371	.209	.213	.333	.609	.298	.259	.466
120°	.452	.215	.314	.520	.937	.369	.424	.787
127.5°	.494	.236	.399	.660	1.153	.447	.553	1.027
135°	.547	.281	.514	.843	1.433	.560	.724	
142.5°	.627	.349	.667	1.071	1.809	.715		
150°	.752	.448	.865	1.352				
157.5°	.936	.581	1.123	1.706				
165°	1.189	.757						
172.5°	1.529	.986						

Table 3b. $\Delta\xi$ vs. $\Delta\theta$ (see Eqs. (7), (8)) for continuous electrostatic channel. $E = 50$ MeV, $\Delta\xi$ — in.

θ° \ Δθ	100 (kV/cm)				150 (kV/cm)			
	15°	45°	75°	105°	15°	45°	75°	105°
30°	.161	.167	.205	.189	.162	.179	.208	.190
45°	.169	.199	.208	.175	.174	.206	.213	.178
60°	.187	.236	.199	.162	.204	.256	.208	.170
75°	.248	.256	.187	.177	.288	.305	.199	.196
90°	.346	.262	.184	.246	.449	.345	.211	.299
105°	.483	.272	.212	.380	.725	.400	.282	.499
120°	.653	.315	.326	.620	1.164	.543	.443	.852
127.5°	.750	.368	.421	.801	1.472	.674	.570	
135°	.869	.449	.547	1.034		.857		
142.5°	1.037	.565	.712	1.328		1.106		
150°	1.276	.723	.927	1.702				
157.5°	1.607	.932						
165°	2.053	1.208						

Table 3c. Δξ vs. Δθ (see Eqs. (7), (8)) for continuous electrostatic channel. E = 51 MeV, Δξ = in.

θ° Δθ	100 (kV/cm)				150 (kV/cm)			
	15°	45°	75°	105°	15°	45°	75°	105°
30°	.166	.186	.237	.224	.169	.189	.240	.226
45°	.175	.223	.249	.209	.181	.232	.257	.213
60°	.215	.276	.244	.203	.234	.303	.258	.214
75°	.293	.327	.236	.230	.344	.398	.259	.214
90°	.435	.366	.247	.310	.550	.511	.295	.262
105°	.668	.412	.320	.479	.913	.659	.423	.388
112.5°	.826	.456	.390	.612	1.174	.780	.535	.638
120°	1.011	.532	.491	.788	1.509	.958	.687	.828
127.5°	1.229	.649	.630	1.017		1.207	.892	
135°	1.504	.817	.813	1.312				
142.5°	1.871	1.043	1.053					
150°		1.344						

Table 4. Arc length, Δs, of a continuous electrostatic channel to produce a $\Delta r = 10.90$ in., $\Delta s =$ in.

θ_o / E(MeV)	15°	45°	75°	105°	ξ(kV/cm)
49	94.65	89.38	81.24	81.22	100
	73.46	78.49	70.72	65.80	150
50	89.35	87.89	79.91	76.41	100
	68.15	76.93	70.09	64.61	150
51	80.63	84.57	78.09	72.77	100
	63.43	73.74	69.25	63.32	150

Table 5a. Δr vs. Δθ for 60°, 150 kV/cm electrostatic channel followed by a 4 kilogauss magnetic channel. E = 50 MeV, Δr = in.

Δθ \ θ_0	15°	45°	75°	105°
60°	1.869	1.907	1.538	1.698
75°	3.122	2.753	2.346	2.775
90°	5.326	3.908	3.872	4.914
105°	8.734	5.897	6.900	9.099
112.5°	11.098	7.471	9.474	12.524
120°	14.228	9.783	13.268	
127.5°		13.333		

Table 5b. Δr vs. Δθ for 60°, 150 kV/cm electrostatic channel followed by a 4 kilogauss magnetic channel. E = 51 MeV, Δr = in.

Δθ \ θ_0	15°	45°	75°	105°
60°	1.990	2.051	1.604	1.749
75°	3.449	3.091	2.448	2.946
90°	6.131	4.541	4.097	5.403
105°	10.660	6.984	7.534	10.354
112.5°	14.053	8.969	10.512	14.548
120°		11.973		

Table 6a. $\Delta\xi$ vs. $\Delta\theta$ for 60°, 150 kV/cm electrostatic channel followed by a 4 kilogauss magnetic channel. E = 50 MeV, $\Delta\xi$ = in.

$\Delta\theta$ \\ θ_0	15°	45°	75°	105°
60°	.202	.256	.208	.170
75°	.287	.304	.198	.182
90°	.452	.346	.211	.300
105°	.753	.411	.293	.516
112.5°	.979	.479	.371	.688
120°		.752		

Table 6b. $\Delta\xi$ vs. $\Delta\theta$ for 60°, 150 kV/cm electrostatic channel followed by a 4 kilogauss magnetic channel. E = 51 MeV, $\Delta\xi$ = in.

$\Delta\theta$ \\ θ_0	15°	45°	75°	105°
60°	.234	.303	.258	.214
75°	.343	.397	.258	.260
90°	.554	.512	.295	.389
105°	.945	.678	.434	.658
112.5°	1.245	.822	.565	.875
120°		1.036		

Table 7a.   Δr vs. Δθ for 45° electrostatic channel, Δr = in.

θ₀ / Δθ	15°	45°	75°	105°
45°	.999	1.068	.935	.923
60°	1.738	1.785	1.428	1.572
90°	3.666	2.616	2.438	3.221
120°	5.436	3.230	4.228	6.678
150°	7.803	5.165	8.992	12.863
157.5°	9.119	6.153	10.930	15.127
165°	11.000	7.456	13.242	
172.5°	13.615	9.134	16.034	
180°		11.242		
187.5°		13.854		
195°		17.093		

Table 7b.   Δξ vs. Δθ for this configuration, Δξ = ir.

θ₀ / Δθ	15°	45°	75°	105°
45°	.174	.206	.213	.178
60°	.203	.254	.207	.169
90°	.410	.314	.194	.272
120°	.861	.402	.320	.696
150°	1.725	.872	.866	1.838
157.5°	2.161	1.116	1.114	2.318
165°	2.735	1.436	1.426	
172.5°		1.850	1.821	
180°		2.376		
187.5°		3.046		

Table 8a. Δr vs. Δθ for continuous electrostatic channel with rotation against the spiral, Δr = in.

Δθ \ θ₀	0°	30°	60°	90°
45°	.989	1.066	.982	.889
60°	1.854	1.900	1.715	1.537
90°	4.973	4.241	3.520	4.091
120°	10.620	8.069	8.529	11.097
127.5°	12.856	10.048	11.086	14.187
135°	15.932	12.896	14.612	

Table 8b. Δξ vs. Δθ for this configuration, Δξ = ir.

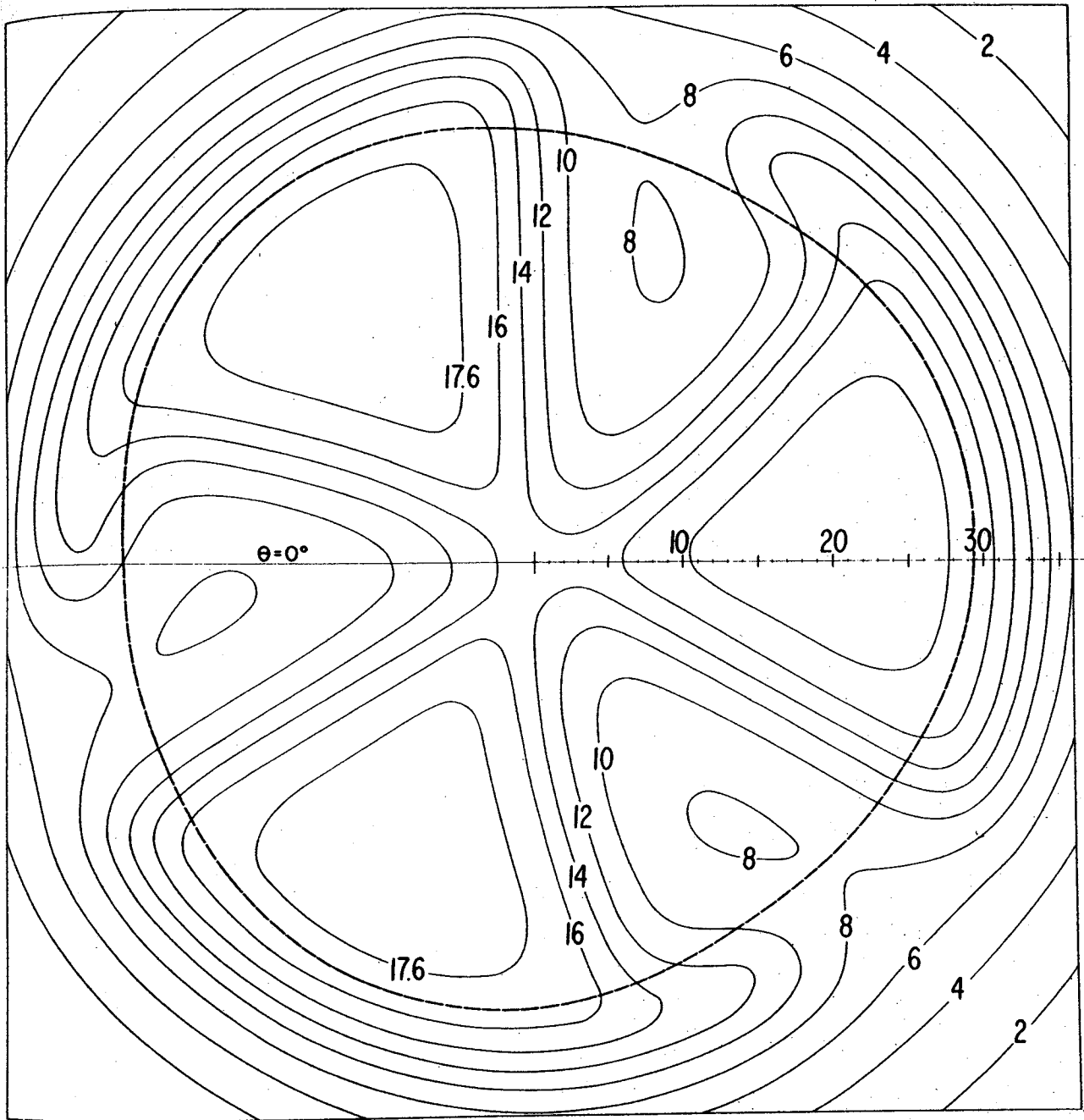| Δθ \ θ₀	0°	30°	60°	90°
45°	.174	.181	.193	.210
60°	.185	.219	.222	.200
90°	.396	.314	.271	.318
120°	.876	.631	.609	.843
127.5°	1.121	.809	.789	1.092
135°		1.049	1.030	

Fig. 1. Contour map of the magnetic field obtained from Run 187 of magnet measurements. The datum Θ=0° is shown, and the 49 MeV proton equilibrium orbit is shown by the heavy dashed line. Field contours are noted in kilogauss and radial scale is inches.
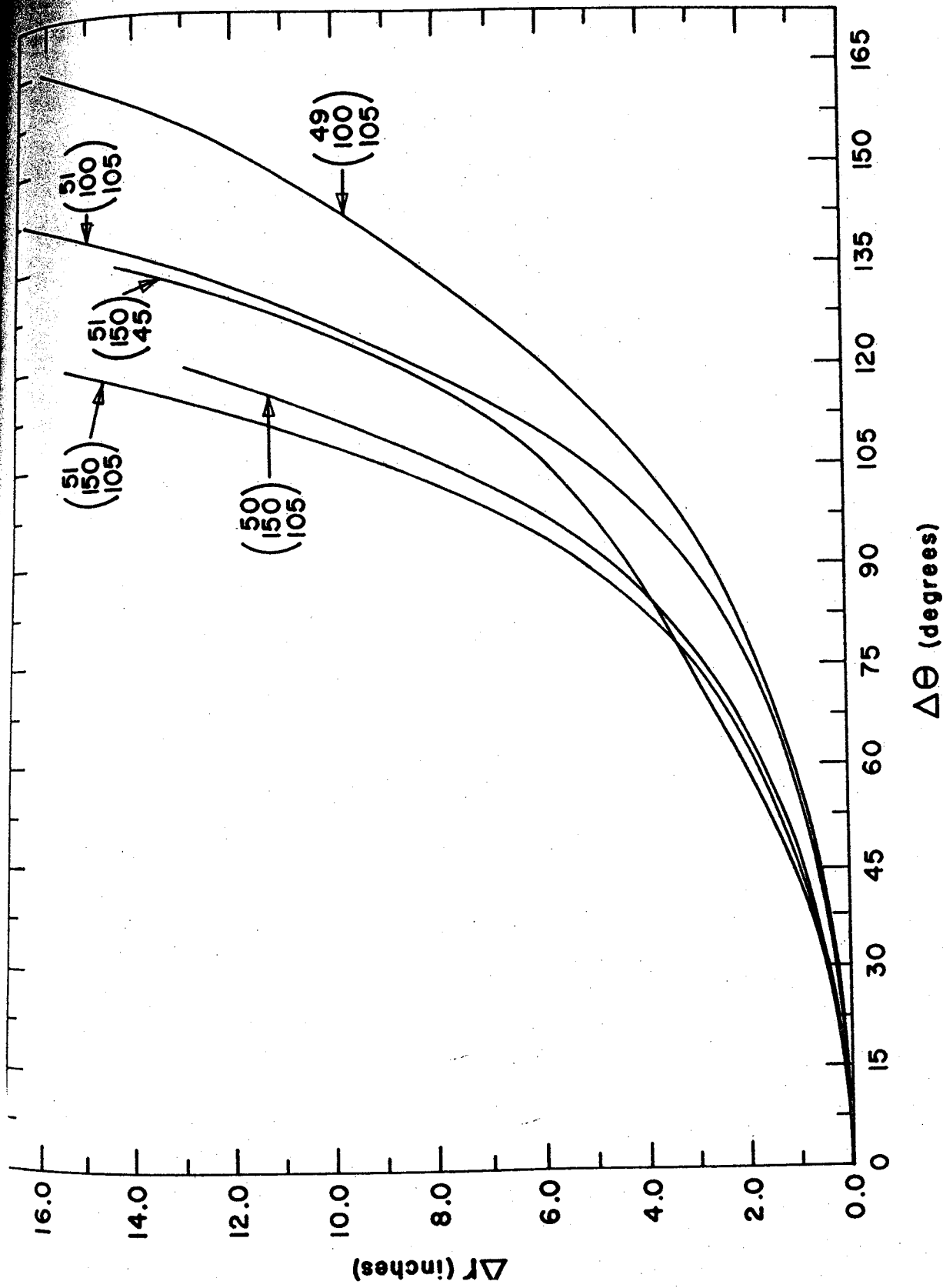
Fig. 2. Δr vs. $\Delta \Theta$ (see Eq. (5)) for the continuous electrostatic channel to the edge of the magnetic field. The triplet of numbers labeling each curve denotes respectively the energy, E, in MeV, the electric field strength, F, in kV/cm, and the initial deflector azimuth Θ_0 in degrees.
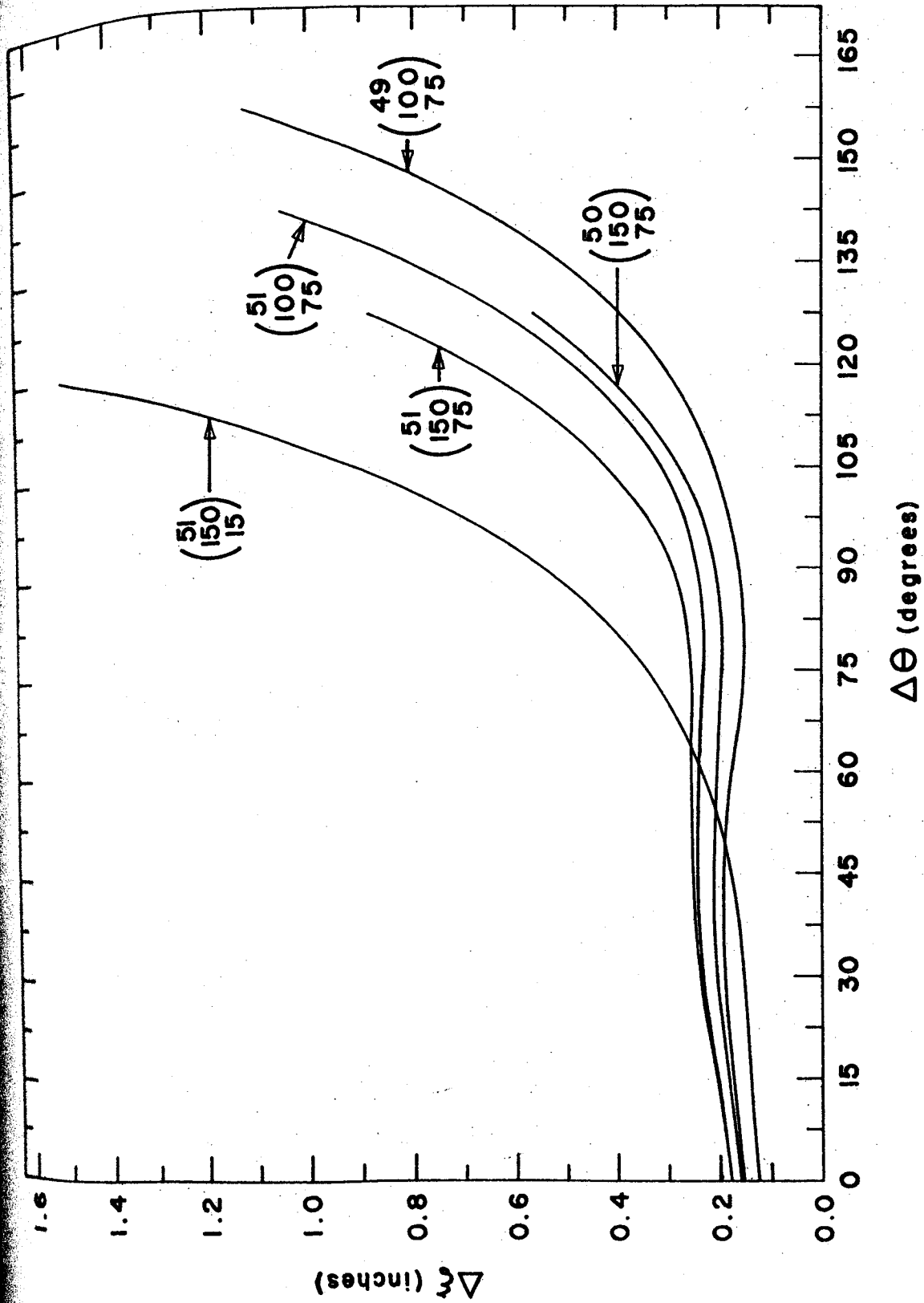
Fig. 3. $\Delta \xi$ vs. $\Delta \Theta$ (see Eqs.(7),(8)) for continuous electrostatic channel to the edge of the magnetic field. The triplet of numbers labeling each curve denote the same parameters as in Fig. 2.
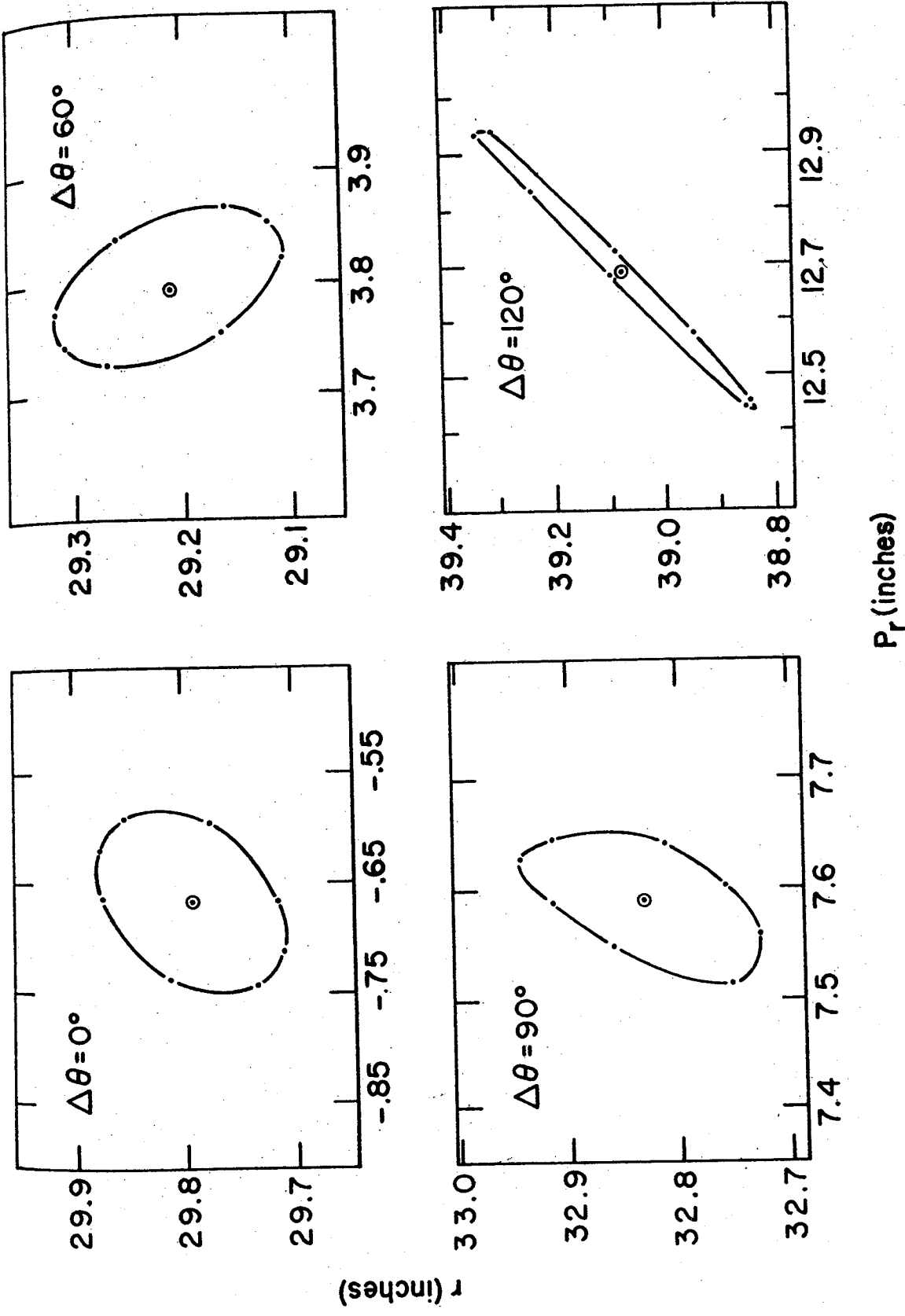
Fig. 4. Evolution of radial phase-space area traced through a continuous 150 kV/cm electrostatic channel with $\theta_0 = 75°$ and E=50 MeV.

Fig. 5. Maximum axial displacement $|Z_{max}|$ vs. $\Delta\theta$ for values of θ_0, F and E. In the figure $\mathcal{E}$ =F in the text for values of electric field strength.

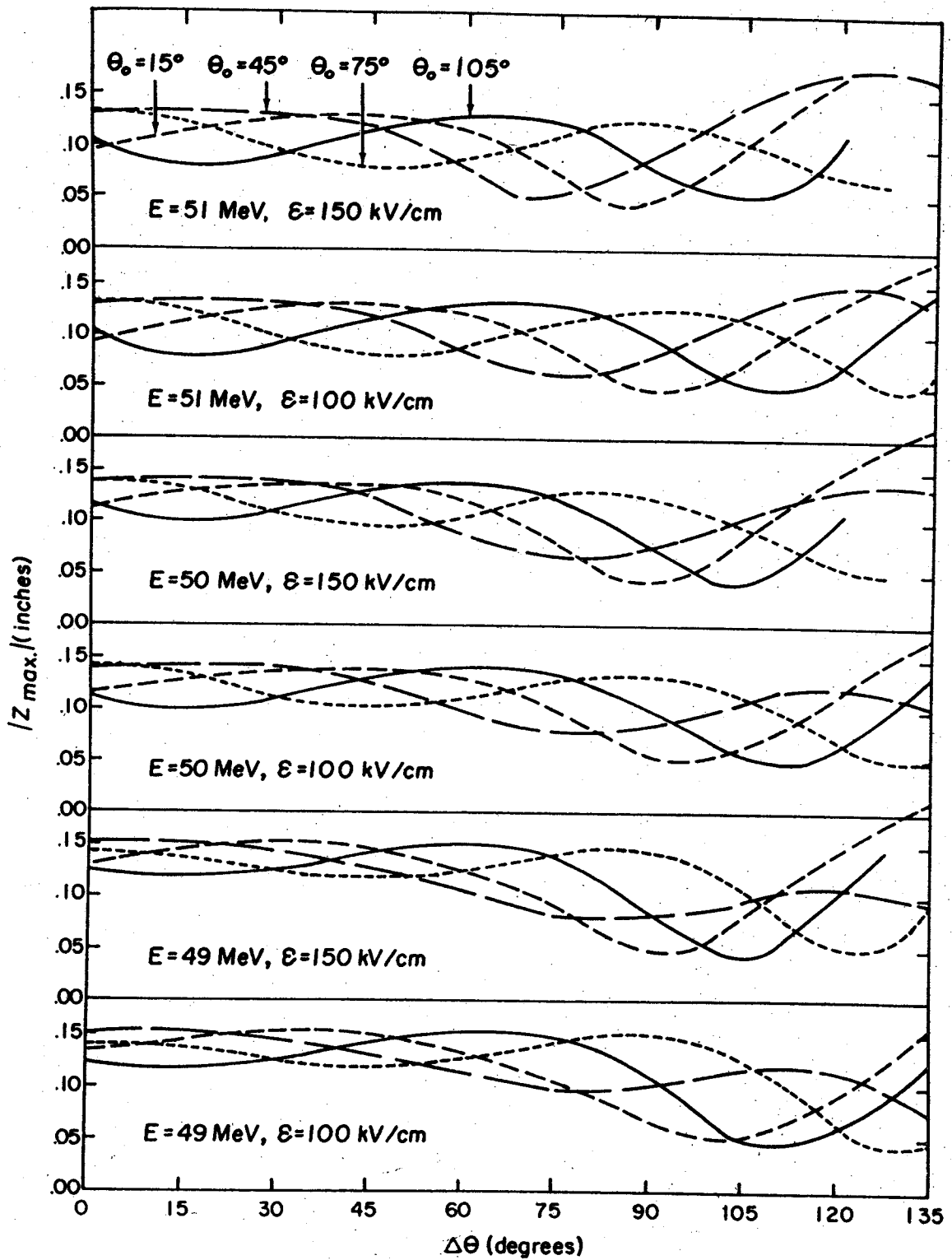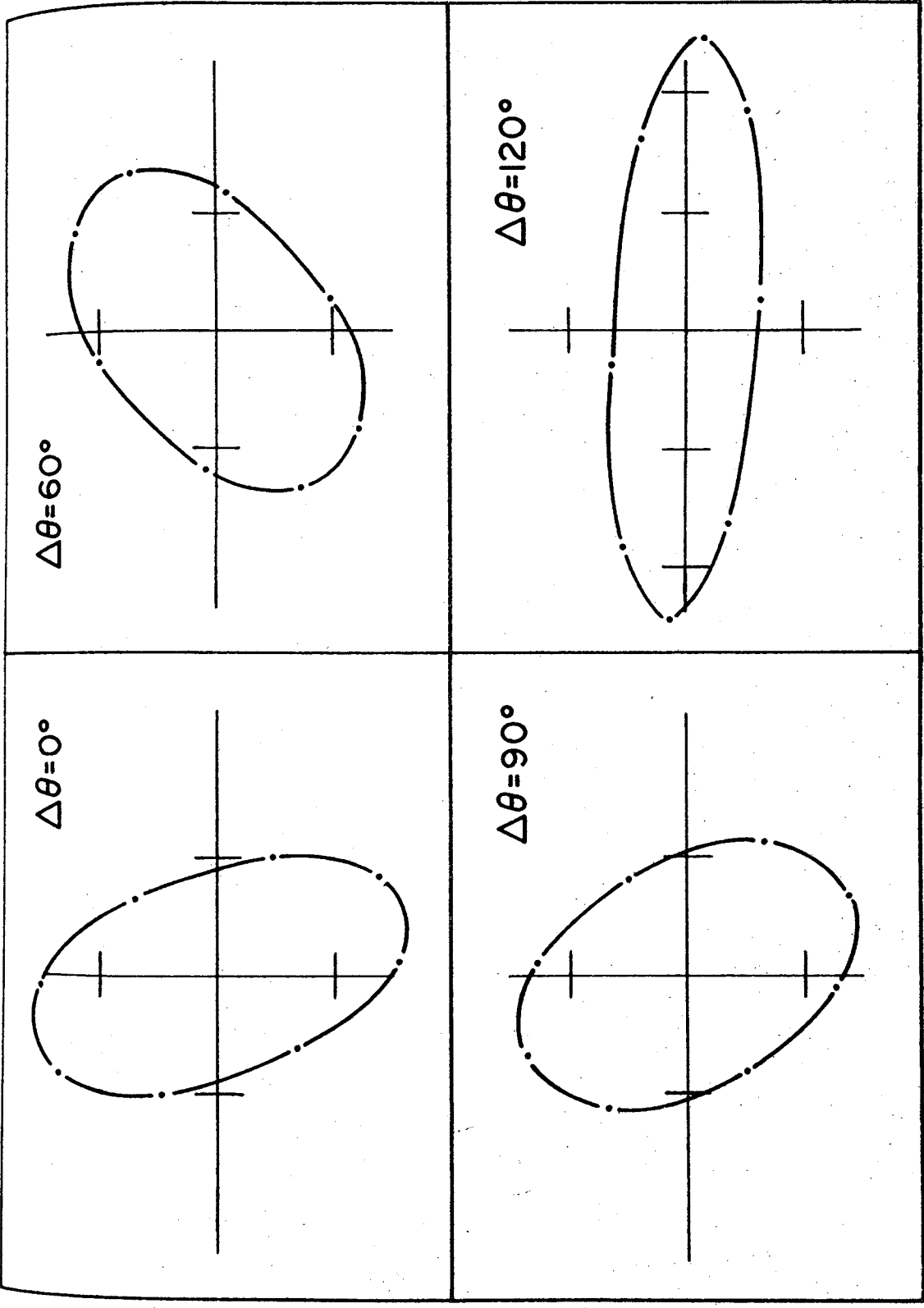Fig. 6. Evolution of axial phase-space area associated with the central ray traced through a continuous 150 kV/cm electrostatic channel with $\theta_o=75°$ and E=50 MeV (same parameters as Fig. 4). (Z scale is arbitrary.)
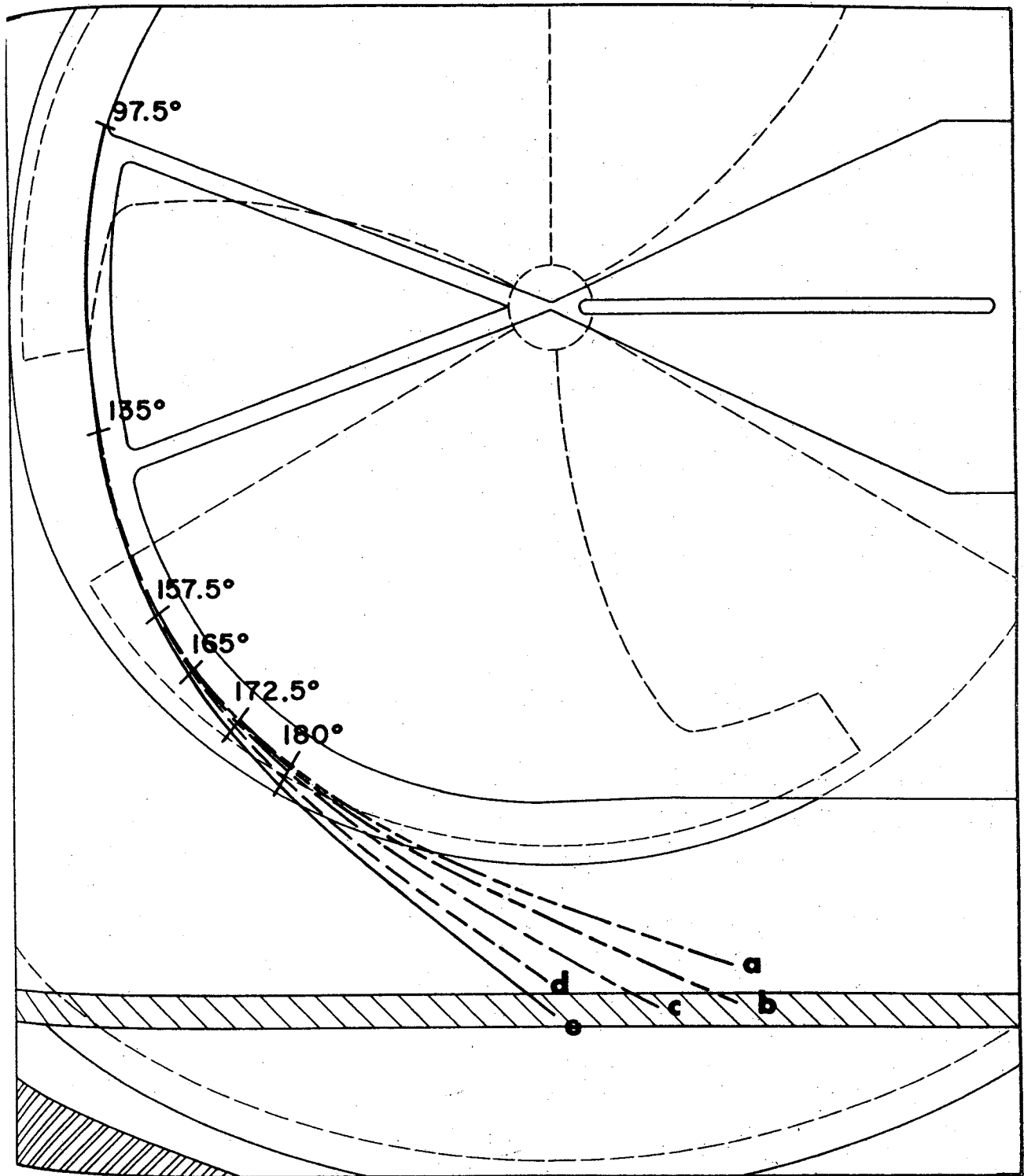
Fig. 7. 51 MeV central ray through various combinations of a 150 kV/cm electrostatic channel and a 4 kilogauss magnetic channel, all with $\Theta_0 = 97.5^\circ$. Curves "a"-"d" represent a 37.5° electrostatic channel with $\Theta_{om} = 180^\circ$ (curve "a"), $\Theta_{om} = 172.5^\circ$ (curve "b"), $\Theta_{om} = 165^\circ$ (curve "c"), $\Theta_{om} = 157.5^\circ$ (curve "d"). Curve "e" depicts a 60° electrostatic channel with $\Theta_{om} = 165^\circ$. Dees shown are for 50 MeV protons.

Fig. 8. 50 MeV central ray through various combinations of a 150 kV/cm electrostatic channel and a 4 kilogauss magnetic channel for the same cases as given in Fig. 7.
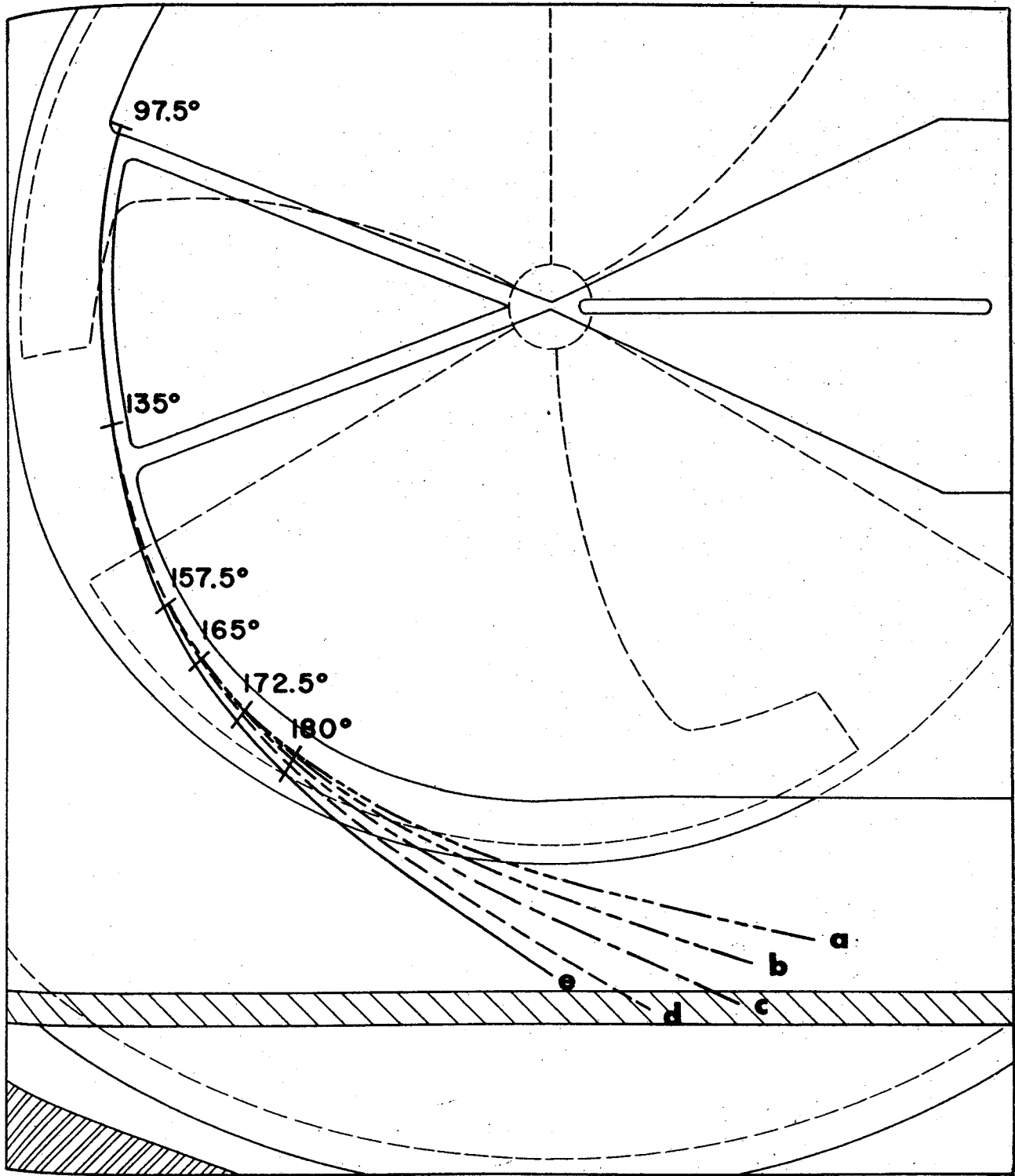
III. VARIABLE-ENERGY, MULTI-PARTICLE DEFLECTION

A series of computer runs was made to study the variable-energy, multi-particle aspect of the cyclotron with respect to deflection. In these studies low energy protons and high energy C^{4+} ions were tracked through the deflector. A comparison between central rays for these ions through the deflector and those of the previous section indicates what changes, if any, in the shape or position of the deflector might be necessary.

There are two requirements that must be satisfied in order to have different orbits coincide for deflection. The first is that the various beams all arrive at the same deflector radius, and the second is that the various orbits follow the same trajectory within the deflector itself.

If the magnetic field scaled exactly in the deflector region, that is, if the shape of the field is independent of the excitation, then the trajectories of static orbits through the deflector could be made to coincide exactly. A scaling magnetic field would be the case if there were no saturation effects in the magnet. For the M.S.U. cyclotron, the magnetic field was designed so as to minimize as much as possible the effects of magnet saturation in the deflection region.

To note the effects of a scaling magnetic field on the deflection process, consider the following simple analysis. The trajectory of the equilibrium orbit outside the deflector is given by:

$$p = qB(r,\theta)\, \rho_o(r,\theta) \ , \qquad (9)$$

where $B(r,\theta)$ is the magnetic field along the E.O. and $\rho_o(r,\theta)$ is the radius of curvature. If the magnetic field scales, then for an ion of charge q', momentum p', in a field $B'(r,\theta)$ such that:

$$\frac{B'(r,\theta)}{B(r,\theta)} = \frac{p'}{q'}\frac{q}{p} \ ; \qquad (10)$$

then:

$$\rho_o(r,\theta) = \rho_o'(r,\theta) \ ; \qquad (11)$$

that is, the trajectories of static orbits arrive at the same deflector radius.

The second requirement that the two orbits follow the same trajectory in the deflector may be studied by means of the trajectory equation modified for deflector orbits:

$$p = q[B(r_c, \theta) - \frac{F}{v}]\rho(r_c, \theta) \qquad (12)$$

where $\rho(r_c, \theta)$ is the radius of curvature of the central ray; $B(r_c, \theta)$ is the field along the central ray; v is the velocity of the particle; and the electric field, F, is assumed to be perpendicular to the central ray. Assuming the magnetic field along the central ray scales according to Eq. (10), then the trajectories within the deflector will coincide if the term F/v scales in the same way. Namely, the ratio of the electric fields is given by:

$$\frac{F'}{F} = \frac{q}{q'} \frac{p'v'}{pv} . \qquad (13)$$

From Eq. (13) the approximate changes in the electric field strength can be calculated for the various deflection cases. The approximate changes in the magnetic field strength for a magnetic channel can be calculated from Eq. (10).

The low excitation proton magnetic field used for investigating low energy deflection was again obtained from magnet measurements. This magnetic field is designated 192.1 and yields proton equilibrium orbits up to approximately 12 MeV. A contour map of field 192.1

is shown in Fig. 9 with the $\theta = 0°$ datum as shown and the 11 MeV ($\nu_r = 0.950$) E.O. is shown by the heavy dashed line.

As a basis for comparison, high excitation proton orbits initially on the E.O. at 50 and 51 MeV at the initial deflector radii of 29.000 and 29.584 in. respectively were computed through the deflection system in the 187F6 field. The deflection system was specified: $\theta_o = 97.5°$; 60° electrostatic channel, $F = 150$ kV/cm; $\theta_{om} = 165°$, 4 kilogauss magnetic channel to the edge of the magnetic field (see case e of Sec. II-B, Figs. 7 and 8). By determining the energy at which deflection occurs so as to have the initial radii of the orbits coincide, orbits in the 192.1 field with energies of 11.101 and 11.411 MeV have radii at $\theta = 97.5°$ equal to those of 50 and 51 MeV, respectively, in the 187F6 field. Computer runs were then made for the low energy deflection varying the field strength within the electrostatic and magnetic channels in order to match the central rays with those obtained for the high excitation mode. A good match between the central rays for the high and low energy deflection modes was obtained with low energy deflection specified by $F = 35.44$ and 36.21 kV/cm in the 60° electrostatic channel and 1.78

and 1.75 kilogauss in the magnetic channel for the two respective energies. These results agree quite well with Eqs. (10) and (13) with an error of approximately 4%.

Table 9a tabulates differences in radii at $7.5°$ intervals for the pairs of matched central rays. The largest difference between the high and low energy orbits in both cases is about 0.04 in. which is quite small. Also, the matched orbits are heading out of the main magnetic field parallel to within two minutes when tangents are compared. These results indicate that the magnetic field shape is nearly independent of excitation in the deflection region.

To study the effect of ion changes on the deflection process, orbits for C^{4+} ions were computed for the high excitation magnetic field. This magnetic field, designated 187.3, yields C^{4+} equilibrium orbits up to approximately 71 MeV. The 187.3 field is practically the same as the 187F6 field in the non-isochronous region of the field, namely, in the edge region where deflection is being considered. It should be noted that the 187.3 field extends to approximately 33 in. whereas the 187F6 field extends to 45 in.

As a basis for comparison, high energy protons of energy 50 MeV in the 187F6 field were computed through a continuous electrostatic deflector with $\theta_o = 97.5°$ and $F = 150$ kV/cm. Again by choosing the energy at which deflection begins so as to have the initial radii of the orbits coincide, computer studies were then made of central ray deflection for the C^{4+} case. The initial energy so determined was 68.62 MeV for C^{4+} in the 187.3 field. A good match between the 50 MeV proton central ray in the 187F6 field and the 68.62 MeV C^{4+} central ray in the 187.3 field was obtained with an electric field strength within the continuous electrostatic channel of $F = 50.9$ kV/cm. This value of electric field strength agrees quite well with Eq. (13) with an error of approximately 1%. Table 9b tabulates differences between the two orbits for the two different ions. From the table it is seen that the two central rays very nearly coincide, with the largest difference being 0.018 in. The comparison can be carried out only to about 33 in. since the C^{4+} field extends only that far. This good agreement is expected since the two fields are practically identical in the deflection region.

The results indicate that the saturation effects of the magnetic field are reasonably small. Therefore, it

was concluded that for the M.S.U. variable-energy multi-particle cyclotron, deflection could be accomplished by a simple change in channel field strengths with no changes in the shape or position of the deflector apparatus.

Table 9a. Comparison of central ray displacement for
variable-energy, multi-particle deflection.
Protons for high and low magnet excitations.

θ	$r_{192.1}-r_{187F6}$ (11.101-50MeV) (in.)	$r_{192.1}-r_{187F6}$ (11.411-51MeV) (in.)
97.5°	.0008	-.0021
105°	.0221	.0308
112.5°	.0337	.0438
120°	.0192	.0297
127.5°	-.0080	-.0013
135°	-.0320	-.0300
142.5°	-.0404	-.0415
150°	-.0306	-.0330
157.5°	-.0126	-.0148
165°	.0001	.0000
172.5°	.0032	.0060
180°	.0030	.0071
187.5°	.0046	.0067
195°	.0054	.0013
202.5°	.0022	

Table 9b. Comparison of central ray displacement for
variable-energy, multi-particle deflection.
Protons and C^{4+} at the same magnet excitation.

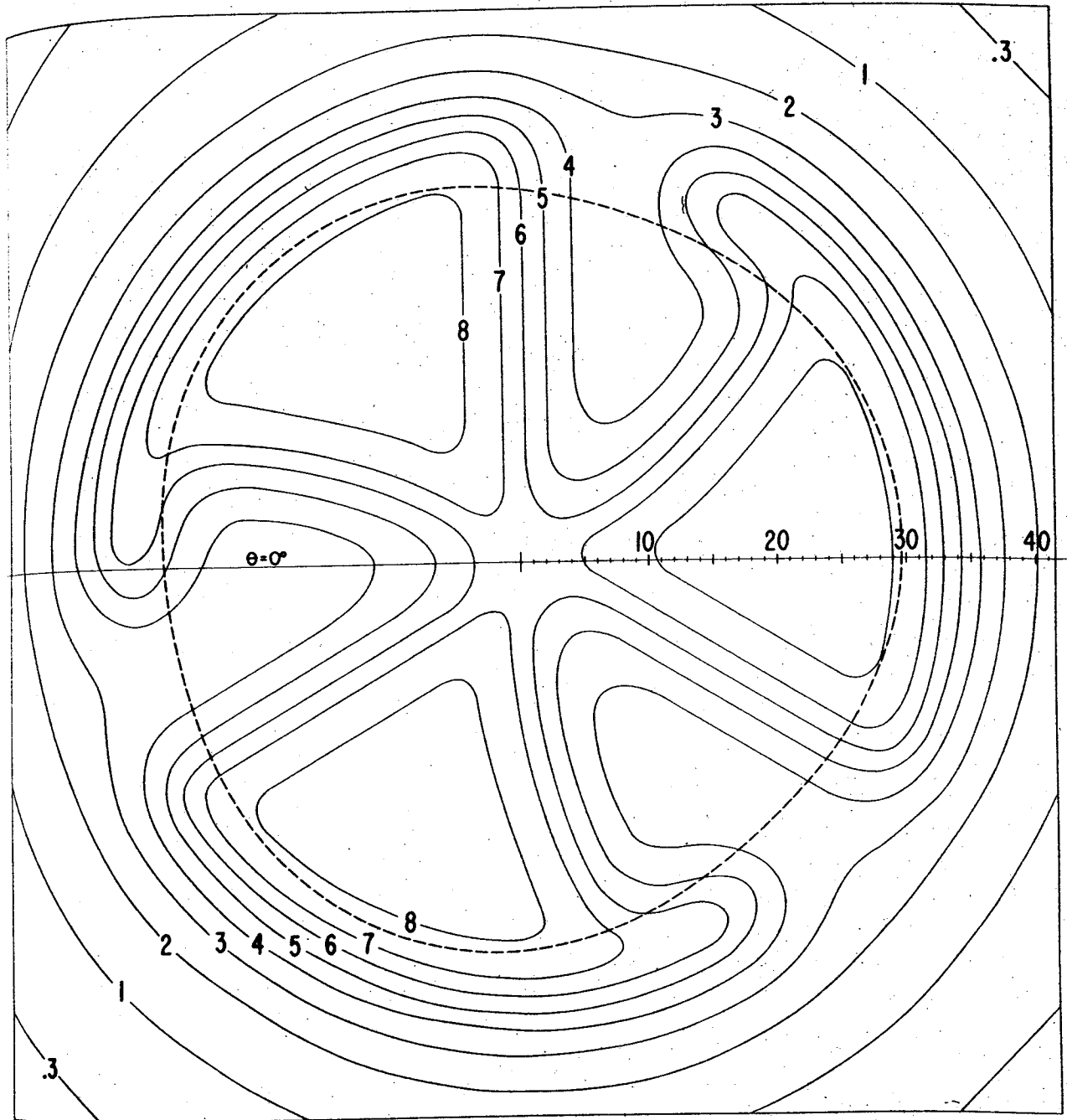| θ	$r_{187.3}-r_{187F6}$ (68.619-50MeV) (in.)
97.5°	.0000
105°	.0018
112.5°	.0027
120°	.0024
127.5°	.0010
135°	-.0016
142.5°	-.0052
150°	-.0094
157.5°	-.0139
165°	-.0181

Fig. 9. Contour map of the magnetic field obtained from Run 192 of magnet measurements. The datum θ=0° is shown and the 11 MeV equilibrium orbit is shown by the heavy dashed line. Field contours are noted in kilogauss and radial scale is inches.

IV. ACCELERATED ORBITS

In the previous sections deflection of orbits initially in the equilibrium orbit at the entrance to the deflector was studied. In the present section orbits accelerated from well below the deflection energy out to the deflection point will be surveyed for the case of the M.S.U. cyclotron. Acceleration is achieved by a two dee system, each dee having 70 kV to ground and an assumed angular width of 135°. Thus, the peak energy gain per turn is $E_1 = 4(70)\cos 22.5° = 259$ kV/turn. The 187F6 magnetic field was used in this study.

Two problems are encountered during acceleration: first, the problem of acceleration through the $\nu_r = 1$ and $\nu_r = 2\nu_z$ resonances which occur prior to deflection; and second, the problem of phase-slip due to acceleration in the non-isochronous edge region. Acceleration through the resonances is a problem due to phase-space distortion introduced and also the difficulty of controlling "field bumps". Regarding the problem of resonances, Fig. 10 shows a plot of $1 - \nu_r$ and $2\nu_z - \nu_r$ vs. energy for the 187F6 field. It is seen that $\nu_r = 1$ at approximately 46.1 MeV and $\nu_r = 2\nu_z$ at approximately 47.8 MeV.

A. Median Plane Motion

Median plane studies were made in order to observe turn separation possible for insertion of the septum-deflector apparatus. The $\nu_r = 1$ resonance may be used in the method of resonant extraction [Ref. 6] in order to yield enhanced turn separation. In this method, the beam is accelerated through the $\nu_r = 1$ resonance where a small, first-harmonic field-bump, $b_1(r,\theta)$, provides a driving force in resonance with the radial oscillations. In this manner the orbits are driven off center. With the value of ν_r dropping sharply in the edge region, the displaced orbit centers undergo rapid orbit precession. Turn separation can thereby be generated which facilitates insertion of the septum-deflector apparatus.

Computer studies were made in order to show the effect of such a bump field. The initial conditions were chosen on the equilibrium orbit at $E = 43$ MeV ($n = 0$) at $\theta = 97.5°$ with an rf phase $\phi_0 = -28.5°$; n denotes turn number. Hereinafter, orbits with this set of initial conditions will be called the central ray and labeled C. In addition, the phase-space, S_r, occupied by the beam was represented initially by the eigen-ellipse defined by eight (x, p_x) coordinates about the equilibrium orbit (radial width normalized to

$\Delta x = 0.22$ in. at $\theta = 97.5°$). The initial value of energy, below both resonance energies, is in the region where the motion is negligibly affected by the non-linearities associated with either resonance. Therefore, an assumption of orbits initially centered at this energy is reasonable. The initial value of rf phase was selected because this value minimized the number of turns necessary to reach $E = 51$ MeV. Such a selection of phase is somewhat arbitrary.

The first set of computer runs was made without a bump field present in order to establish a basis for comparison. Figure 11 shows the evolution of the radial phase-space area, S_r, without a bump field in place. The figure indicates that there is some orbit displacement from the E.O. ($x = p_x = 0$) due, primarily, to the electric gap crossing resonance [Ref. 9]. Also, the orbits are precessing about the instantaneous E.O. From the figure, it is seen that phase-space distortion is small and the orbits remain reasonably well centered about the equilibrium orbit. Figure 12 shows the evolution of the radial phase-space area, S_r, for the case of acceleration with a field bump, $b_1(r,\theta) = h_1(r)\cos\theta$, with $h_1 = 1.0$ gauss (independent of r). The figure shows the greater orbit center displacement produced by

the resonance mechanism and also the greater effect of the precessional motion. This greater orbit center displacement has been gained at the expense of increased phase-space distortion; however, distortion is still quite small. The 1.0 gauss bump field was the only one considered for this study; the results are quite sensitive to the bump field parameters.

Regarding turn separation for insertion of the septum, for the case without the bump field in place, there is no beam separation for successive turns. The minimum beam overlap in this case was 0.07 in. or about 25% of the beam width and occurs between the thirty-third (E = 50.92 MeV) and thirty-fourth (E = 51.06 MeV) turns. With the 1.0 gauss bump field in place, beam separation is possible. To demonstrate this beam separation, Fig. 13 shows the radial phase space, S_r, at the entrance to the deflector as a result of acceleration with the bump field in place. From the figure, it is seen that there is a beam separation of 0.05 in. between the set or orbits at the deflection energy (E = 51.06 MeV, n = 34) and the next closest set of orbits. This turn separation would make insertion of the septum-deflector apparatus feasible.

The second problem encountered during the accelera-
tion process is that of phase-slip during acceleration
in the non-isochronous edge region. The phenomenon of
rapid phase slip in the non-isochronous edge region may
be studied by means of the relation:

$$\sin\phi - \sin\phi_o = S(E) - S(E_o) \ ,$$

$$\tag{14}$$

$$S(E) = \frac{2\pi}{E_1} \int (f_o T - 1)dE \ ;$$

where ϕ is the phase of rf voltage, ϕ_o is the phase at
E_o, f_o is the rf frequency, and $T = T(E)$ is the parti-
cle rotation period.

For isochronous motion, $f_o T \equiv 1$. In this case
$\phi = \phi_o$, or the phase remains constant at its initial
value. In the edge region, however, the average magne-
tic field is decreasing rapidly below the isochronous
value. Under these conditions, $f_o T > 1$, and hence
$\phi > \phi_o$ and is increasing rapidly. The upper limit on
the energy attainable is set by $\phi = 90°$.

There are advantages, however, of accelerating into
the non-isochronous region. As noted earlier in this
section, the precessional motion can be employed to yield
enhanced turn separation. This precessional motion is in
addition to the equilibrium orbit radius gain per turn, δr_e.

The equation for the equilibrium orbit, r_e, can be written as:

$$r_e = R[1 + \eta(\theta)] , \qquad (15)$$

here R is the mean radius of the E.O. and $\eta(\theta)$ specifies the deviation of the E.O. from a circle. The equilibrium orbit radius gain can be written from Eq. (15) as:

$$\delta r_e = \delta R[1 + \eta(\theta) + R\frac{d\eta}{dR}] . \qquad (16)$$

Garren et.al. [Ref. 1] carried out an analysis to show the effect of the sector structure and also the effect of spiral contained in the $\frac{d\eta}{dR}$ factor. For rotation with the spiral the maximum value of δr_e as a function of θ is at $\theta = 112°$ for 50 MeV. The factor δR is connected with the phase slip and may be understood qualitatively by considering the approximate relation between momentum and radius in a magnetic field:

$$p = qB_o(R)R . \qquad (17)$$

From Eq. (17) one has:

$$\frac{\delta p}{p} = \frac{\delta R}{R}(1 + k),$$ (18)

where $k = \frac{R}{B_o}\frac{dB_o}{dR}$ is the field index, and δp and δR are respectively the momentum and radius increments. Since $p \propto E^{1/2}$ in the non-relativistic approximation, then Eq. (18) can be written:

$$\delta R = \frac{1}{2}\frac{R}{(1+k)}\frac{\delta E}{E}.$$ (19)

Eq. (19) can be employed to correlate radius gain per turn with energy gain per turn since δE can be written $\delta E = E_1 \cos\phi$. Therefore, Eq. (19) can be written including the phase factor as:

$$\delta R = \frac{1}{2}\frac{R}{(1+k)}\frac{E_1 \cos\phi}{E}.$$ (20)

It should be noted that this δR contains nothing on the radius gain from the precessional motion or from the sector structure. Since $(1+k) \approx \nu_r^2$ decreases rapidly in the edge region, increased turn separation can be gained by accelerating into the edge region. However, ϕ increases rapidly in the non-isochronous region due to

phase slip. The limiting value of $\phi = 90°$ would correspond to the condition where the energy gain and hence the radius gain are zero.

The computer runs for acceleration studies also give results for the phase. The case discussed below is for central ray acceleration with the 1.0 gauss bump field in place and with the same initial conditions as given previously. The table below tabulates at $\theta = 97.5°$: the turn number, n; the energy, E; the phase, ϕ; δr_e determined from E.O. data; δr the total radius gain containing the precessional motion; and δE the energy gain for the particular turn.

n	E(MeV)	ϕ	δr_e(in.)	δr(in.)	δE(keV)
0	43.00	−28.50°	.072	———	———
5	44.15	−24.80°	.074	.066	233
9	45.10	−21.03°	.077	.072	240
13	46.07	−16.21°	.081	.075	247
17	47.08	− 9.84°	.086	.078	254
21	48.11	− 1.04°	.093	.113	258
25	49.14	10.92°	.103	.167	256
29	50.13	28.33°	.114	.024	235
32	50.75	46.48°	.125	−.008	190
33	50.92	54.64°	.109	−.090	166
34	51.06	63.17°	.097	.425	137

The results presented in the table indicate that although the energy $E = 51.06$ MeV is somewhat below the $\phi = 90°$ limiting value the phase has slipped almost 92° in 34 turns and is slipping quite rapidly. From the table, δr_e increases to a maximum prior to the deflection energy and then starts to decrease due to the rapid phase slip. At $n = 34$, δr_e is approximately 35% greater than its initial value at 43 MeV. The results for δr for $n = 34$ show the large effect of orbit center displacement demonstrating how the two effects of radius gain through acceleration into the non-isochronous region and radius gain through orbit center precession can be added to yield increased turn separation. From these results, it can be concluded that it is advantageous to accelerate into the edge region since increased turn separation can be gained in spite of phase slip.

Using the group of orbits, S_r, obtained in the median plane acceleration studies above, further studies of deflection were made. The initial conditions for deflection were the phase space area shown in Fig. 13 obtained with the bump field in place after 34 turns to an energy of 51.06 MeV. At the entrance to the deflector the transverse beam width was 0.27 in. whereas in the static case (Sec. II) the beam width was 0.2 in.

This phase-space area was then tracked through various deflector channels. Figure 14 shows the radial envelopes of the beam through various deflector channels. Each beam envelope had the same initial coordinates at $\theta = 97.5°$. Curve "a" depicts deflection due to a continuous 100 kV/cm electrostatic channel; curve "b" represents a 37.5°, 150 kV/cm electrostatic channel followed by a 37.5° coasting period and then a 4 kilogauss magnetic channel; curve "c" depicts deflection by a 60°, 100 kV/cm electrostatic channel followed by a 7.5° coasting period and then a 4 kilogauss magnetic channel; curve "d" represents a continuous 150 kV/cm electrostatic channel; and curve "e" depicts a 60°, 150 kV/cm electrostatic channel followed by a 7.5° coasting period and then a 4 kilogauss magnetic channel. The figure shows the beam spreading due to the radially defocusing impulse at the magnet hill. The beam width at the edge of the field for the slowest deflection system (case a) is 2.06 in. compared with 1.06 in. for the fastest deflection system (case e).

In addition, Fig. 15 shows the central ray of each of these envelopes plotted on the M.S.U. cyclotron layout. From the figure it is seen that a continuous 100 kV/cm electrostatic channel (case a) does not deflect

the beam clear of the vacuum chamber while deflection
by means of the other channel arrangements deflects the
beam into the approximate region desired.

It is of interest to compare these results for de-
flection after acceleration with those for static de-
flection of Sec. II. The main difference between the
two cases is the fact that the accelerated orbits are
displaced approximately 0.2 in. outward from the equili-
brium orbit at the entrance to the deflector. For the
case of deflection after acceleration with the contin-
uous 150 kV/cm electrostatic deflector (case d), central
ray displacement was 11.19 in. at $\Delta\theta$ = 112.5°; whereas
for the static deflection case, central ray displacement
was 10.86 in. at this $\Delta\theta$. The ratio of the beam width
at the edge of the field to the beam width at the en-
trance to the deflector was 4.46 for accelerated orbits
and 3.34 for static orbits for this deflector arrange-
ment. The general features of deflection for accelerated
orbits are quite comparable to those obtained for the
static orbits of Sec. II.

The above results together with subsequent studies
have established the following set of parameters for the
beam deflection system for the M.S.U. cyclotron: 60°,
120 kV/cm electrostatic channel followed by a 7.5° coast-
ing period and then a 37.5°, 3 kilogauss magnetic channel.

B. Coupled Radial and Axial Motion

The coupling effect is due to the higher order non-linear terms in the Hamiltonian. Third-order terms like xz^2 in the Hamiltonian produce an effect on the radial motion of a resonant driving force proportional to z^2 at $\nu_r = 2\nu_z$. This term produces an effect on the axial motion of an alternating gradient type driving force proportional to the orbit center displacement tending to produce axial "blow-up" at $\nu_r = 2\nu_z$. The $\nu_r = 2\nu_z$ resonance is the most important of the coupling resonances since it is the lowest order such resonance traversed. There are also third-order terms like $xz^2\cos 3\theta$ that can produce a radial resonant displacement and an axial alternating gradient driving force at $\nu_r + 2\nu_z = 3$. However, this resonance is not traversed in the 187F6 field. Values of $\nu_r + 2\nu_z$ range from 1.38 to 2.63 over the range of 43 to 51.4 MeV. The fourth-order terms like x^2z^2 in the Hamiltonian produce a frequency shifting effect in both the radial and axial oscillations. The main effect of the frequency shifting terms is to alter the values of ν_r and ν_z from their nominal values. The shift in ν_r is proportional to z^2, and the shift in ν_z is proportional to x^2. At resonance the effect of the frequency shift is to detune the focusing oscillations from their resonant values. Also, the x^2z^2 term in the Hamiltonian

provides an alternating gradient driving force when $2\nu_r = 2\nu_z$. For the 187F6 field the $2\nu_r = 2\nu_z$ resonance is traversed at approximately 50.2 MeV. Also, fourth-order terms like $x^2 z^2 \cos 3\theta$ are present in the Hamiltonian leading to a resonant effect at $2\nu_r + 2\nu_z = 3$. This resonance is traversed at approximately 49 MeV and again at about 51.3 MeV with the value of $2\nu_r + 2\nu_z$ remaing close to the resonance value in this energy range. However these fourth-order resonances are not expected to be as serious as the third-order coupling resonance.

For coupled motion the radial and axial phase-space areas are no longer each constant in area as they would be if no coupling were included. In the case of coupled motion the total, six-dimensional phase area $\int dr\, dp_r\, dz\, dp_z\, dE\, d\phi$ is constant. The radial and axial projections of this total phase space can not only change shape but also vary in area.

In coupled motion studies a modified version of the General Orbit Code was employed in order to more realistically treat the coupled motion between the radial and axial oscillations. The equations of motion integrated in this modified code are derivable from a Hamiltonian corresponding to a vector potential correct through second order in z. Since the equations of motion

are derivable from a Hamiltonian, the motion is, in principle, physically realizable. This modified code agrees quite well with the MURA code Ill Tempered Five [Ref. 10] in comparison runs.

The orbits representing the axial phase space, S_z, occupied by the beam initially corresponded to an eigen-ellipse defined by eight (z, p_z) coordinates about the median plane values $z = p_z = 0$ (axial width normalized to $\Delta z = 0.86$ in. at $\theta = 97.5°$ and $E = 43$ MeV). This value of initial axial width is approximately four times the initial radial width. In the following accel-eration studies the remaining initial conditions were the same as the median plane study above with the 1.0 gauss bump field in place.

For comparison Fig. 16 depicts the maximum axial amplitude vs. energy for various approximations to the axial motion. Curve "a" depicts adiabatic linear motion associated with the instantaneous equilibrium orbit at the particular energy with no coupling included. From this curve, it is seen that the axial amplitude decreases due to the adiabatic damping of the axial motion. For this particular case, maximum axial amplitude occurs at approximately $E = 39$ MeV. Curve "b" in Fig. 16 depicts the axial amplitude associated with the central ray for

accelerated motion with the standard General Orbit Code
which includes coupling only of radial into axial
motion. From this curve it is seen that the instability
due to the $\nu_r = 2\nu_z$ coupling resonance is quite pro-
nounced with the maximum axial amplitude occuring at
approximately 49.1 MeV or 1.3 MeV after the resonance.
Curve "c" of Fig. 16 depicts the axial amplitude asso-
ciated with the central ray for acceleration with the modi-
fied General Orbit Code which includes coupling of
radial to axial motion and axial to radial motion. From
the figure it is seen that the position of the coupling
resonance is well-defined by the jump in axial height
just after passing the coupling resonance. However, the
axial blow-up due to the resonance for this case is less
than case "b" since the effects of back coupling are in-
cluded. For both case "b" and case "c" the axial motion
exhibits adiabatic damping prior to the resonance energy.
Above approximately 49.2 MeV the resonance effect dimin-
ishes, and the adiabatic damping causes the axial ampli-
tude to again decrease. The high frequency oscillations
(especially above ~49 MeV) in curves "b" and "c" cannot
be resolved, but they may be due to the higher order
coupling effects. For both cases "b" and "c" the maximum
z-amplitude associated with the resonance is not larger

than the initial z; this result is quite sensitive to the amount of radial amplitude.

The coupled motion was further studied by tracking, with the modified orbit code, orbits whose radial coordinates initially occupy the radial eigen-ellipse, S_r of the median plane study above (see Fig. 12) and whose axial coordinates occupy the axial eigen-ellipse, S_z, and with the 1.0 gauss bump field in place. By computing the orbits for each of the eight points on the radial eigen-ellipse associated with each of the four points on the axial eigen-ellipse (axial symmetry about $z = p_z = 0$), the effects of the coupling mechanism could be studied. The remainder of the initial conditions were the same for this study as those in the above median plane study (see Sec. IV-A).

Figure 17 shows typical x-p_x phase-space evolutions associated with given points on the axial eigen-ellipse. In the figure the solid curve is for median plane motion ($z = p_z = 0$) as shown previously in Fig. 12. The dashed curve corresponds to a (z,p_z) coordinate initially on the semi-major axis of the axial ellipse, and the dashed-dotted curve is for an initial (z,p_z) coordinate on the semi-minor axis of the axial eigen-ellipse. From the figure it is seen that the three phase-space areas are

only slightly displaced relative to each other after passing through the $\nu_r = 1$ resonance (n = 15, E = 46.57 MeV). This indicates the effect of the frequency shifting term is small. At the twentieth turn (E = 47.84 MeV) the three phase space areas are displaced relative to each other due to the resonant displacement effect at $\nu_r = 2\nu_z$. Also, the two phase-space areas associated with the two (z, p_z) points are pulling apart from each other with the median plane phase-space overlapping these two. At n = 25 where the z-amplitude from Fig. 16 is largest due to the resonance, the areas of the two phase-space figures associated with points on the axial ellipse are less than the area for the median plane case. From n = 25 through the remainder of the acceleration to n = 33, the three phase space areas continue to precess with approximately the same relative position and area.

To observe the coupling of the radial into the axial motion, Fig. 18 shows the evolution of the axial phase-space associated with given points of the radial eigen-ellipse. In the figure, the solid curve is the axial phase-space associated with the central ray enclosed by the circle in Fig. 17; the dashed curve corresponds to the point enclosed by the square in Fig. 17; and the dashed-dotted curve corresponds to the point enclosed by

the triangle in Fig. 17. These two particular points on the radial eigen-ellipse were chosen since they correspond initially to the semi-major and semi-minor axes of the radial eigen-ellipse that remain farthest off-center throughout acceleration. Prior to approximately $n = 20$ the axial phase-space areas very nearly coincide. From Fig. 18 it is seen that at $n = 25$ the axial phase-space areas associated with the off-center orbits have greater axial width and a larger area than the phase-space area associated with the central ray. At the higher energies ($E \simeq 50$ MeV) the axial phase-space associated with the off-center orbits is becoming distorted while the phase-space for the central ray remains undistorted.

The radial and axial "smearing" of the beam due to the coupling effect clearly affects beam deflection. Figure 19a shows r-p_r phase-space areas at the entrance to the deflector ($n = 34$). The three areas in the figure correspond to the same (z, p_z) points as in Fig. 17. The solid curve representing the median plane result is the same as shown in Fig. 13. From Fig. 19a it is seen that the beam occupies a wider radial width due to the coupling effect. For purely median plane motion the radial beam width is approximately 0.27 in. Due to the coupling effect, however, the beam is spread to a radial width of about 0.36 in.

Results were also obtained regarding the spread in energy and phase at the entrance to the deflector. It should be noted that all of the orbits had the same initial conditions for energy and phase at $n = 0$. Tabulated below are results at $n = 34$ for maximum and minimum values of energy and phase for each of the three phase-space areas shown in Fig. 19a.

	E_{max}(MeV)	E_{min}(MeV)	ϕ_{max}	ϕ_{min}
$z = p_z = 0$	51.0612	51.0391	64.79°	62.79°
semi-major (z, p_z)	51.1347	51.0970	60.12°	57.15°
semi-minor (z, p_z)	51.0869	51.0495	64.46°	61.25°

These results indicate that the final values of energy and phase are correlated with the axial motion. The effect of the axial motion is indirect in that the axial motion first couples into the radial motion, and then the differences in the radial displacement produce differences in the energy and phase.

Figure 19b shows the axial phase-space areas at the entrance to the deflector for the same (r, p_r) conditions of Fig. 18. From Fig. 19b it is seen that the axial width of the beam is also smeared due to the coupling effect. For central ray motion the axial width is approximately

0.35 in.; while for orbits that are off-center, the axial width is approximately 0.49 in. which is still much less than the initial axial width of 0.86 in. at 43 MeV.

The results indicate that the $\nu_r = 2\nu_z$ coupling resonance can be traversed under the proper conditions without beam destroying instability. However, a large axial spread as the beam passes through the coupling resonance causes the beam to spread radially. As a result of this radial spreading, the axial amplitude must be restricted if real turn separation is to be obtained. Since the coupling effect goes as z^2, this restriction is probably not serious.
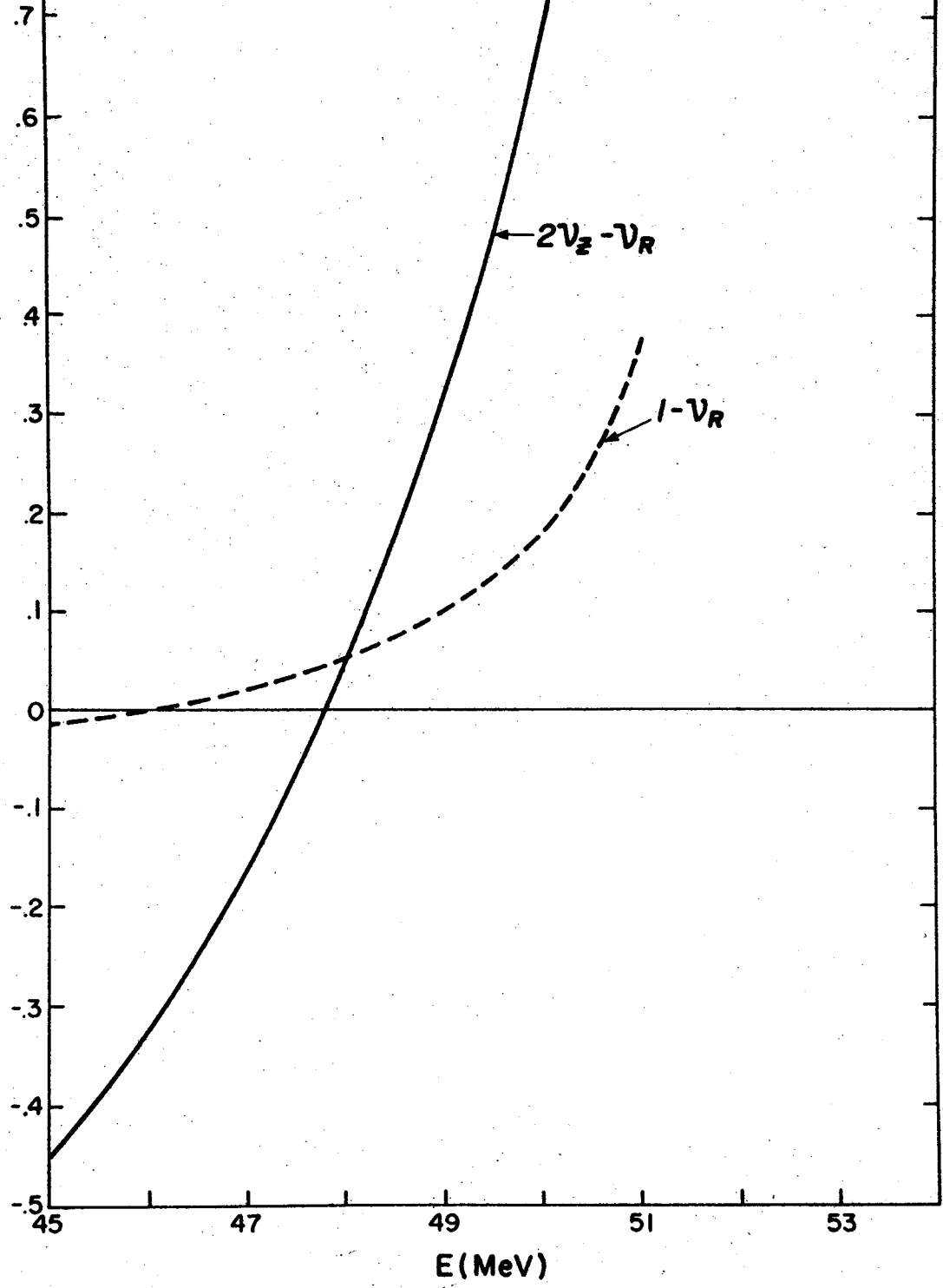
Fig. 10. $(1-\nu_r)$ and $(2\nu_z-\nu_r)$ vs. Energy in edge-region of 187F6 field; $\nu_r=1$ at 46.1 MeV and $\nu_r=2\nu_z$ at 47.8 MeV.
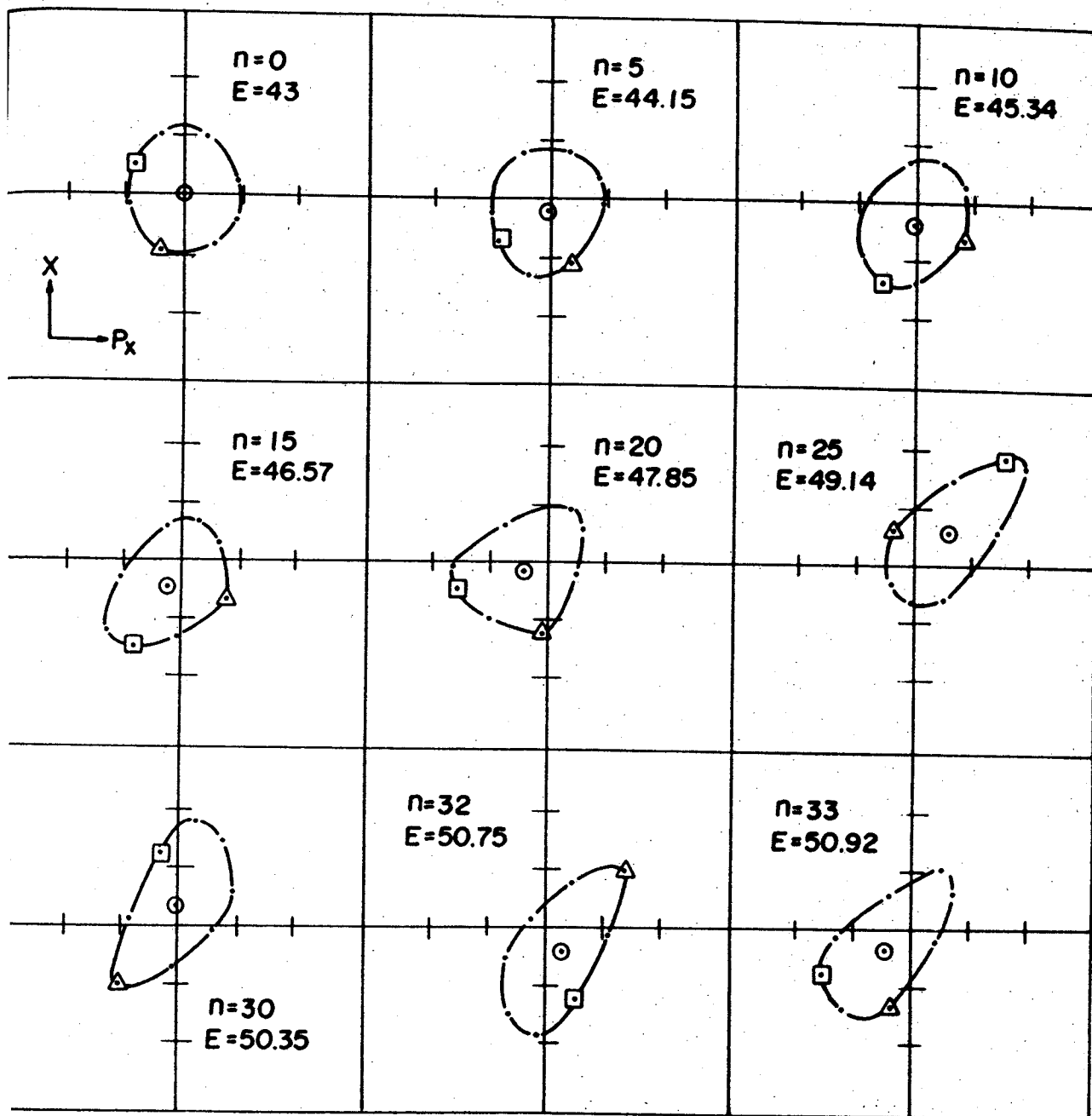
g. 11. Evolution of radial phase-space area at $\Theta = 97.5°$ from 43 to 50.92 MeV with no bump eld included. Each scale division denotes 0.1 inch.
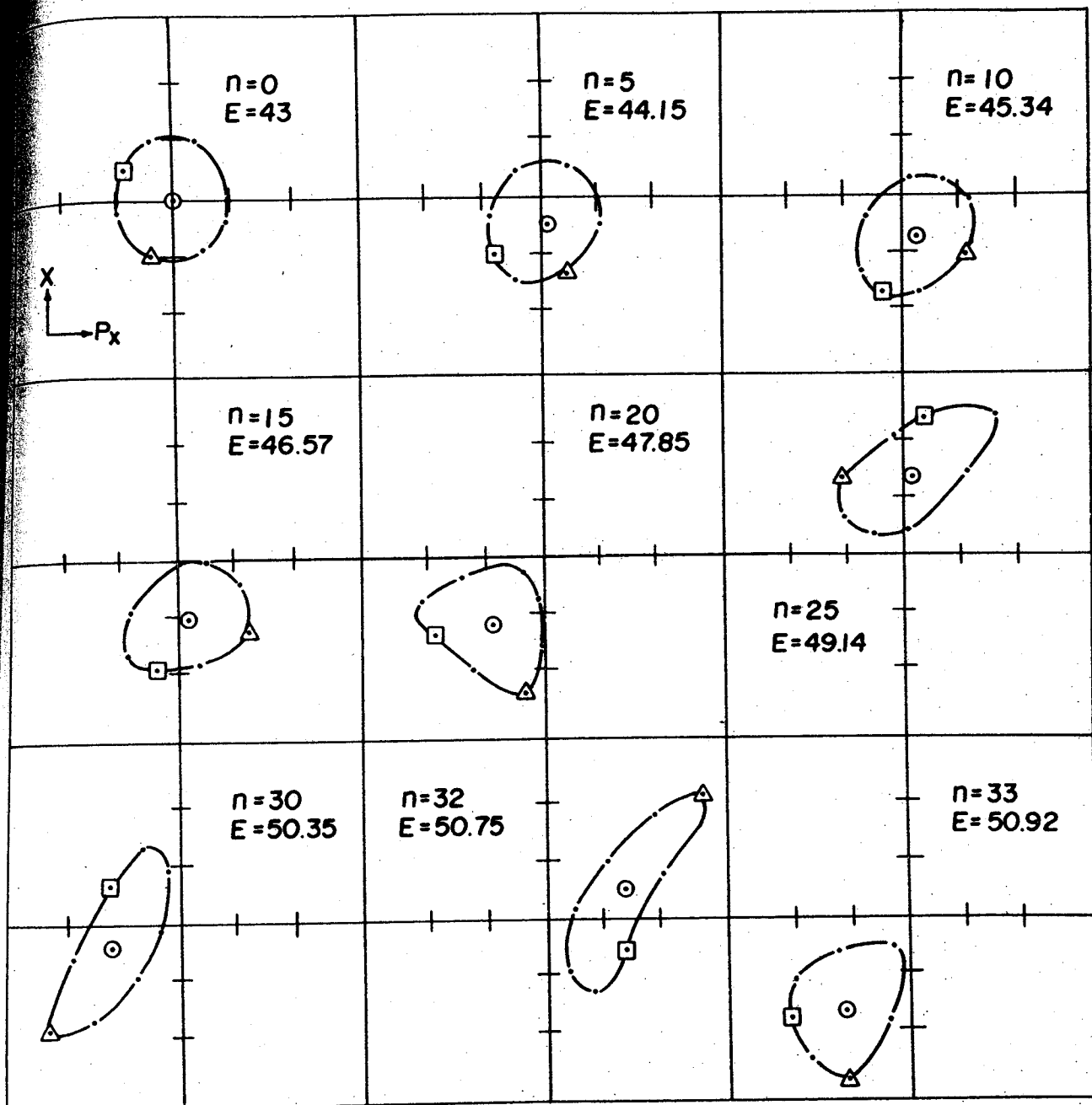
Fig. 12. Evolution of radial phase-space area at θ=97.5° from 43 to 50.92 MeV with the 1.0 gauss bump field in place. Each scale division denotes 0.1 inch.
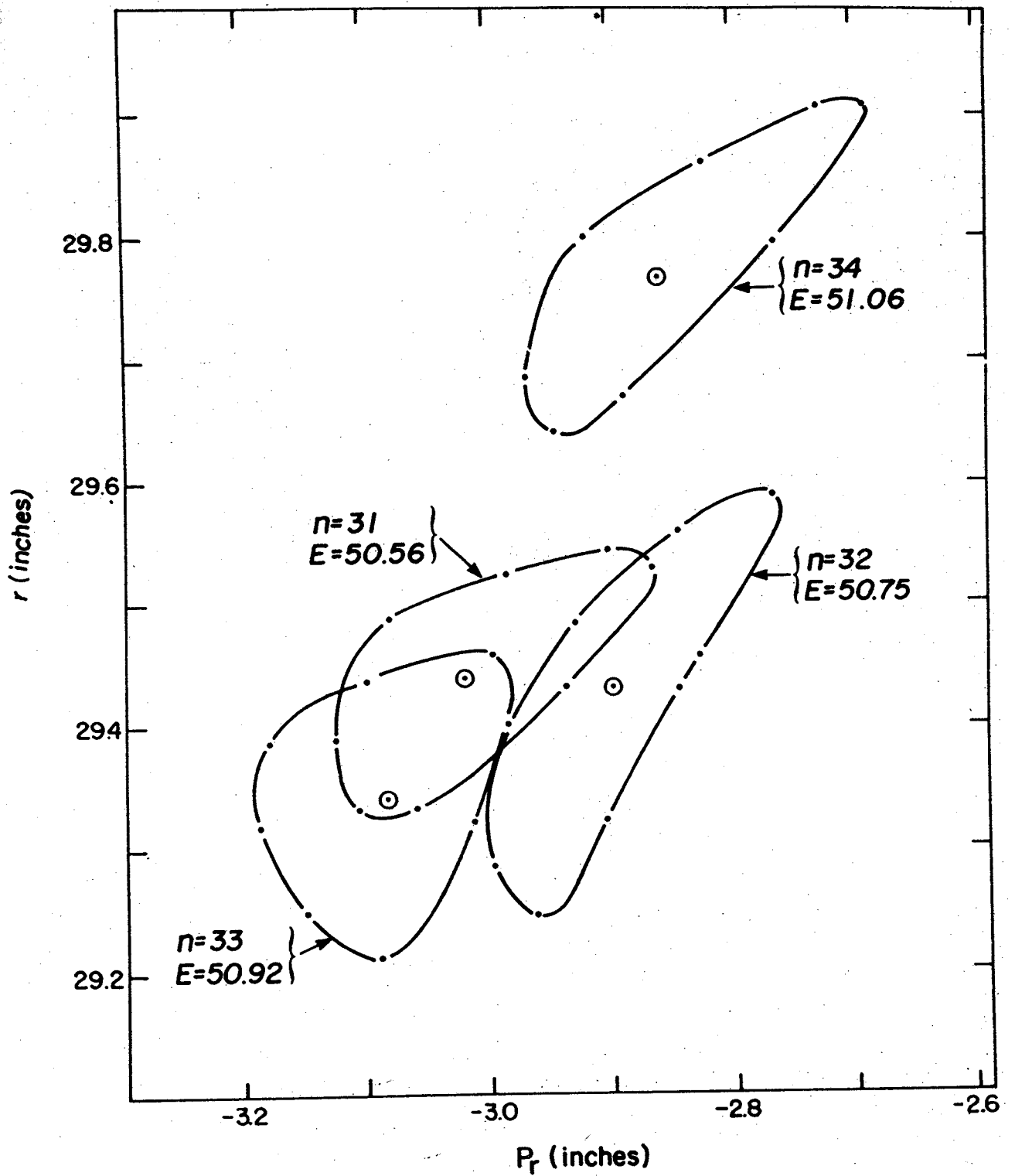
Fig. 13. (r, p_r) locations of orbits on turn n=34 (θ=97.5°) where deflector chan nel begins and on previous turns n=31,32,33.
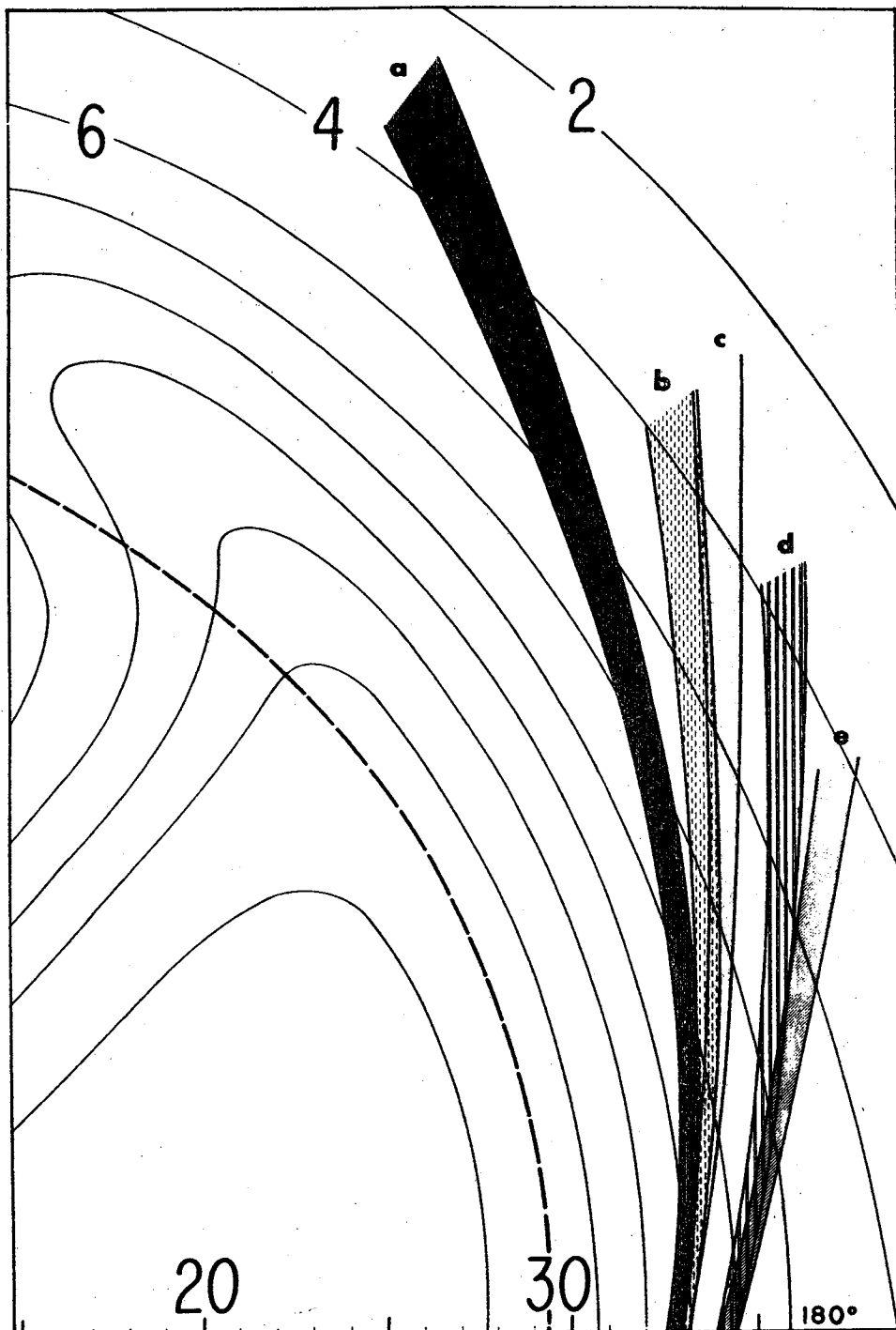
Fig. 14. Radial envelopes through various deflectors with initial conditions
for all envelopes being the phase-space areas on turn n=34 shown in Fig. 13.
Datum θ=180° is shown. The various curves depict deflection by means of: "a",
a continuous 100 kV/cm electrostatic channel; "b", a 37.5°, 150 kV/cm electro-
static channel, 37.5° coasting period, 4 kilogauss magnetic channel; "c", a
60°, 100 kV/cm electrostatic channel, 7.5° coasting period, 4 kilogauss mag-
netic channel; "d", a continuous 150 kV/cm electrostatic channel; "e", a 60°,
150 kV/cm electrostatic channel, 7.5° coasting period, 4 kilogauss magnetic
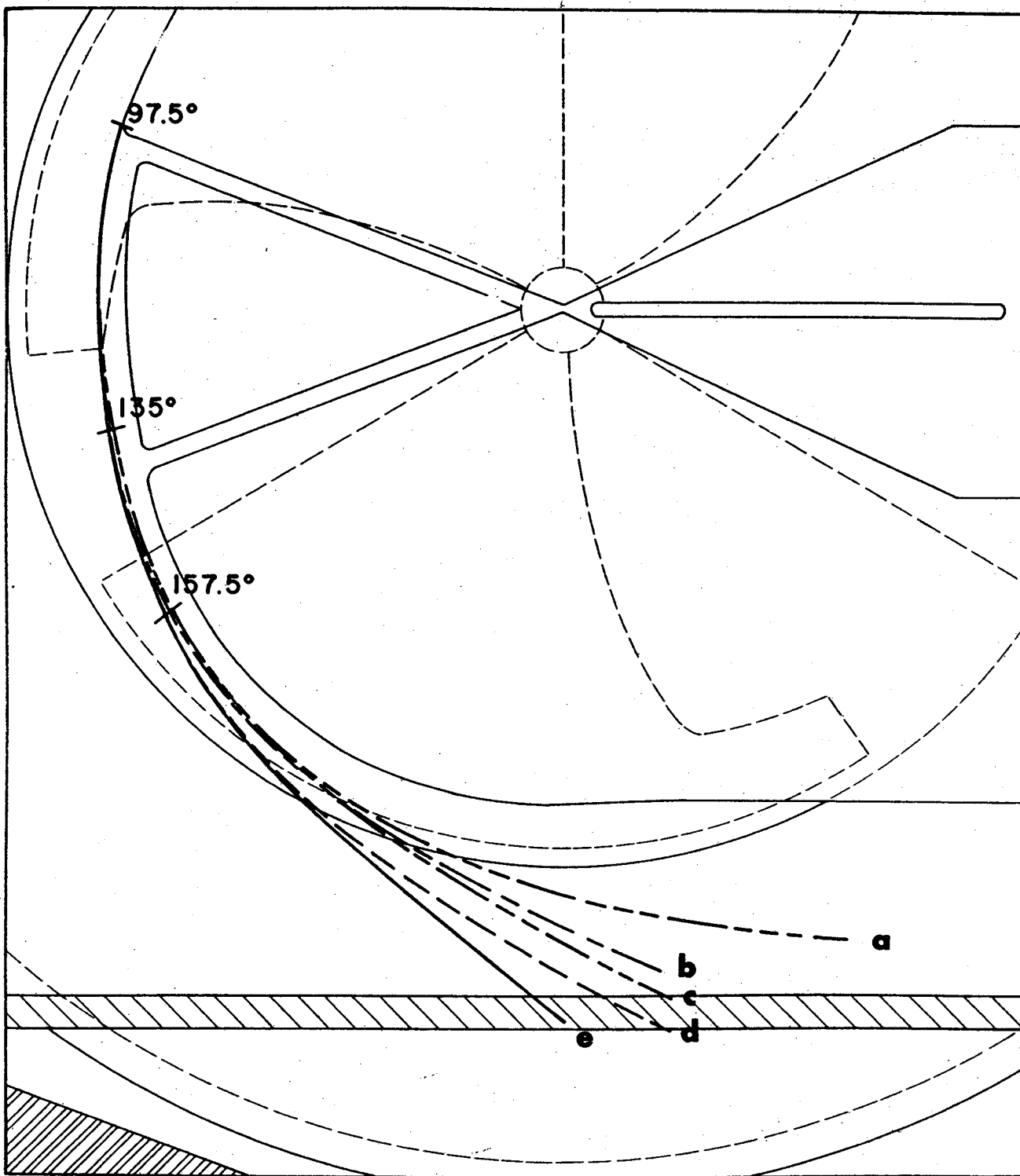channel.

Fig. 15. Central ray associated with each of the radial envelopes as shown in Fig. 14.
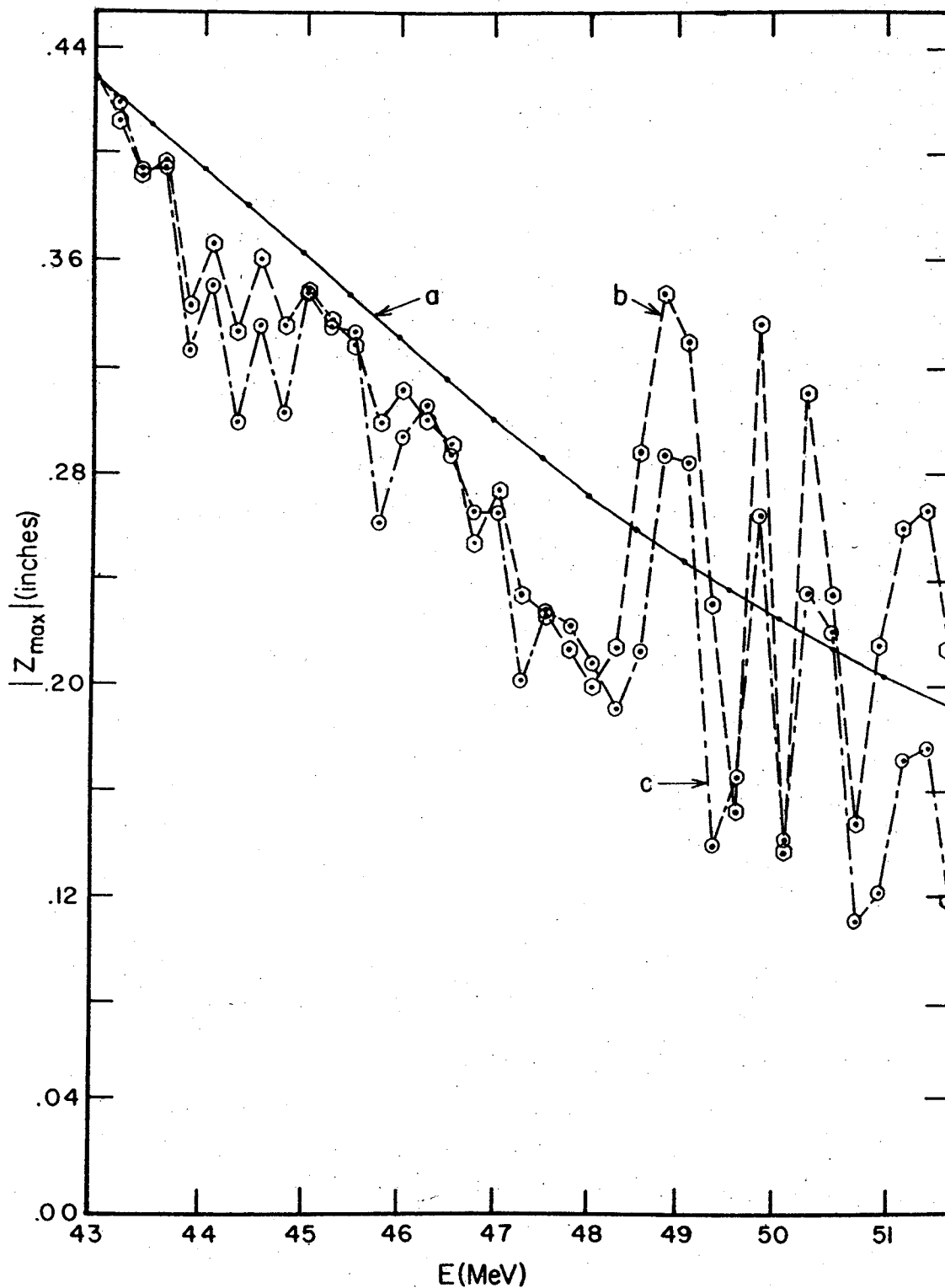
Fig. 16. $|Z_{max}|$ vs. energy obtained for various approximations to the axial motion. Curve "a" is for purely linear motion associated with the equilibrium orbit with no coupling included; curve "b" is for accelerated motion associated with the central ray with coupling of radial to axial motion only; curve "c" is for accelerated motion associated with the central ray with coupling of radial to axial and axial to radial motion included.
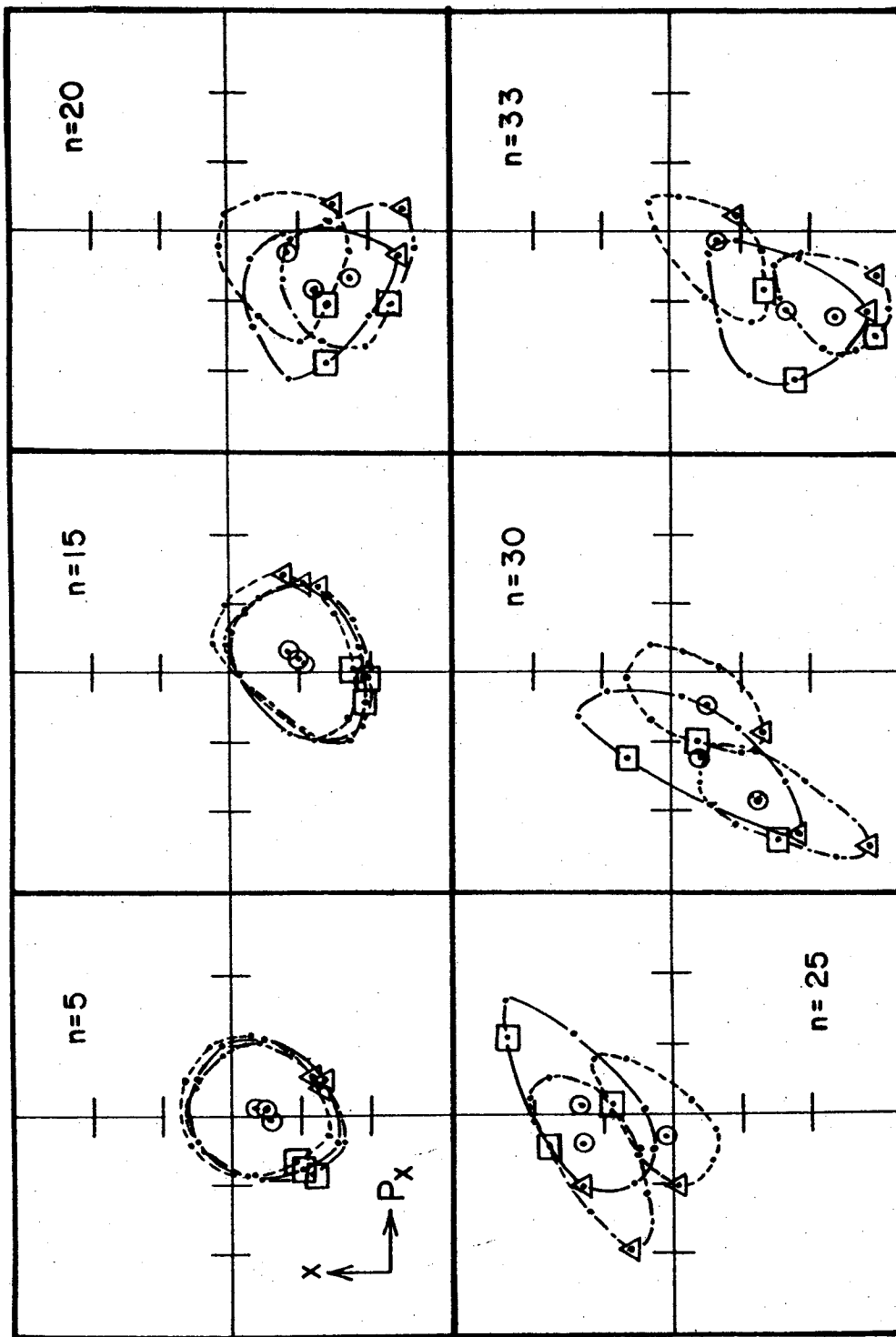

Fig. 17. Evolution of radial phase-space area associated with various points of axial phase-space area. Solid curve denotes median plane ($z=p_z=0$) motion; dashed curve corresponds to a (z,p_z) coordinate initially on the semi-major axis of the axial eigenellipse; dashed-dotted curve corresponds to a (z,p_z) coordinate initially on the semiminor axis of the axial eigen-ellipse. $\sigma=97.5°$, each scale division denotes 0.1 inch.
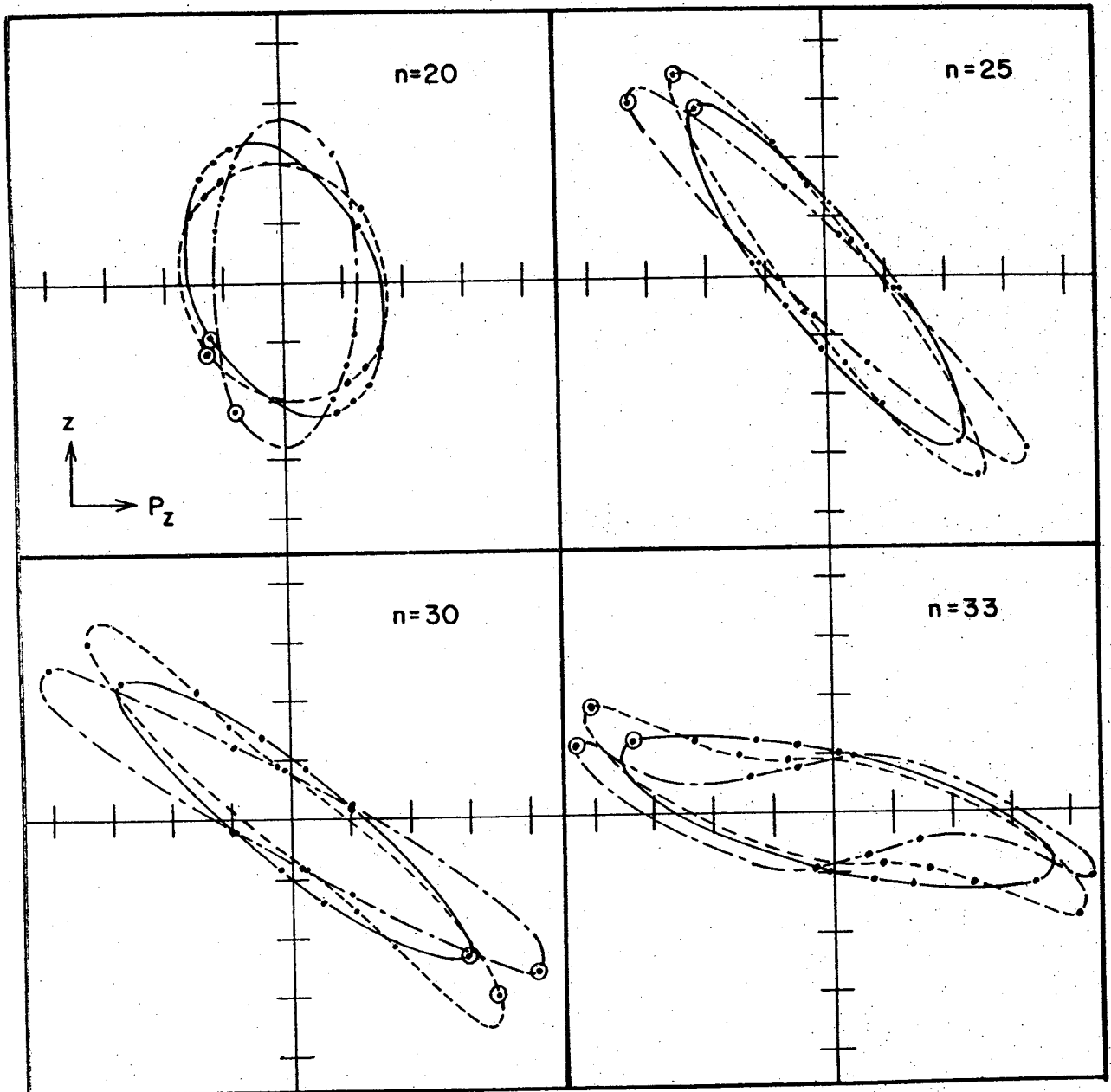
Fig. 18. Evolution of z-p_z axial phase-space area associated with various points of radial phase-space area. Solid curve denotes motion associated with central ray (circled point of Fig. 17); dashed curve denotes motion associated with semi-major axis of radial eigen-ellipse (point enclosed by square in Fig. 17); dashed-dotted curve denotes motion associated with semi-minor axis of radial eigen-ellipse (point enclosed by triangle in Fig. 17). Each scale division denotes 0.1 inch, $\theta = 97.5°$.
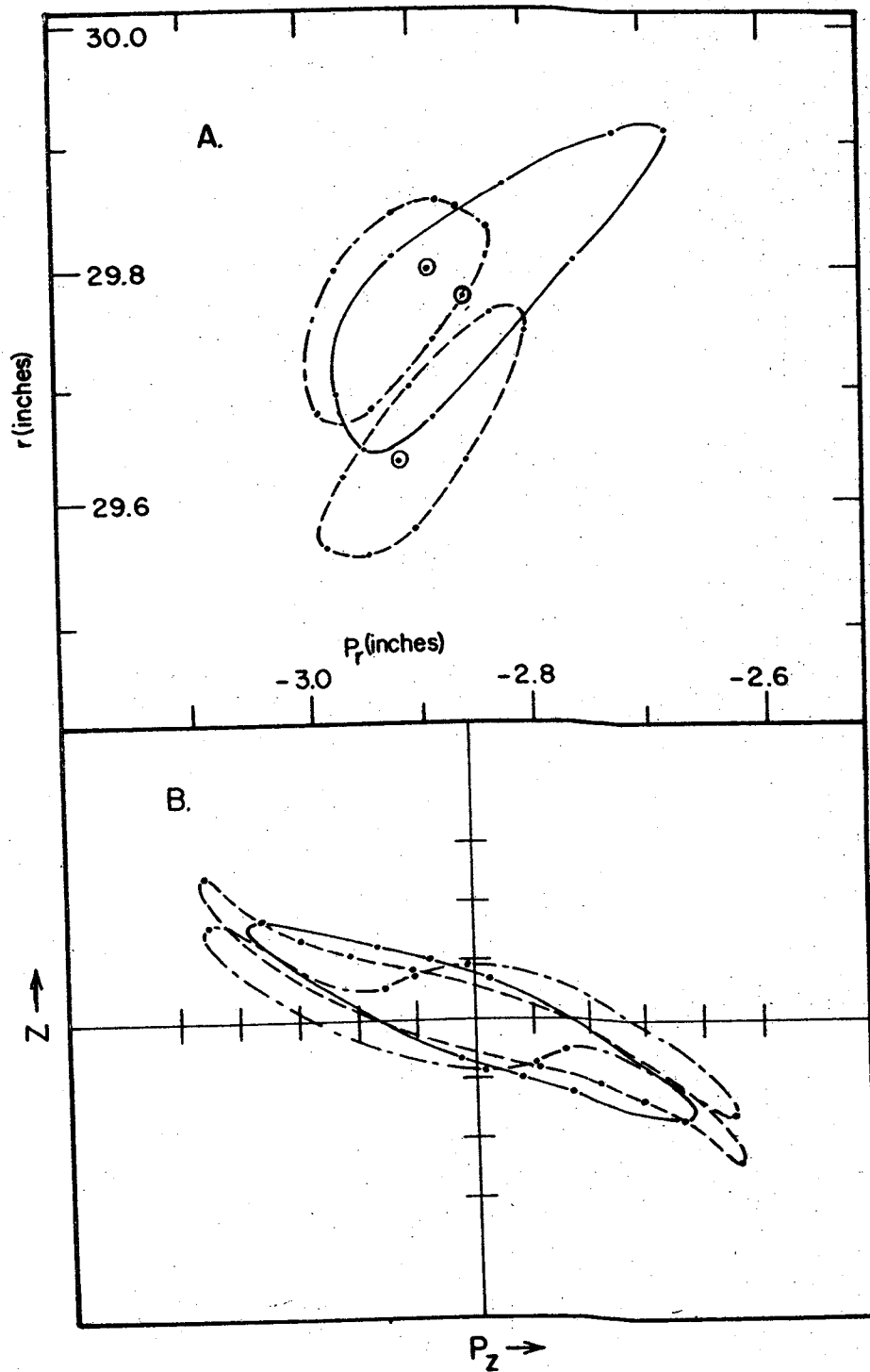
Fig. 19. a). r-p$_r$ phase-space area at entrance to deflector chan-
nel (n=34, Θ=97.5°) for various points of axial phase-space area
as given for Fig. 17. b). z-p$_z$ phase-space area at entrance to
deflector channel for various points of radial phase-space area as
given for Fig. 18. Each scale division denotes 0.1 inch, Θ=97.5°.

REFERENCES

1. A. A. Garren, D. L. Judd, L. Smith and H. A. Wilax, Nucl. Instr. and Meth. 18, 19 (1962), 525.

2. D. A. Harragan, A. R. Mayhook, W. Walkinshaw, An Account of Preliminary Computer Studies of Extraction in a Variable Energy Cyclotron NIRL/R/37 (VEC No. 5).

3. T. I. Arnette, H. G. Blosser, M. M. Gordon and D. A. Johnson, Nucl. Instr. and Meth. 18, 19 (1962), 343.

4. H. L. Hagedoorn and N. F. Verster, Nucl. Instr. and Meth. 18, 19 (1962), 201.

5. L. Smith and A. Garren, Orbit Dynamics in the Spiral-Ridged Cyclotron (Lawrence Rad. Lab., Berkeley, Calif., Jan. 12, 1959).

6. M. M. Gordon and H. G. Blosser, Proc. Int. Conf. on Sector-Focused Cyclotrons & Meson Factories (CERN, April 23-26, 1963, CERN 63-19), 236.

7. H. G. Blosser, Proc. Int. Conf. on Sector-Focused Cyclotrons & Meson Factories (CERN, April 23-26, 1963, CERN 63-19), 270.

8. H. L. Hagedoorn and N. F. Verster, Proc. Int. Conf. on Sector-Focused Cyclotrons & Meson Factories (CERN, April 23-26, 1963, CERN 63-19), 228.

9. M. M. Gordon, Nucl. Instr. and Meth. 18, 19 (1962), 268.

10. E. Z. Chapman, Midwestern Universities Research Association Report MURA-457 (1958).